Burial of the polar magnetic field of an accreting neutron star – I. Self-consistent analytic and numerical equilibria

D. J. B. Payne[★] and A. Melatos

School of Physics, University of Melbourne, Parkville, VIC, 3010. Australia

ABSTRACT

The hydromagnetic structure of a neutron star accreting symmetrically at both magnetic poles is calculated as a function of accreted mass, M_a, and polar cap radius, starting from a centred magnetic dipole and evolving through a quasi-static sequence of two-dimensional, Grad–Shafranov equilibria. The calculation is the first to track fully the growth of high-order magnetic multipoles, due to equatorward hydromagnetic spreading, while simultaneously preserving flux-freezing and a self-consistent mass–flux distribution. Equilibria are constructed numerically by an iterative scheme and analytically by Green functions. Two key results are obtained, with implications for recycled pulsars. (i) The mass required to reduce significantly the magnetic dipole moment, 10^{-5} M$_\odot$, greatly exceeds previous estimates ($\sim 10^{-10}$ M$_\odot$), which ignored the confining stress exerted by the compressed equatorial magnetic field. (ii) Magnetic bubbles, disconnected from the stellar surface, form in the later stages of accretion ($M_a \gtrsim 10^{-4}$ M$_\odot$).

Key words: accretion, accretion discs – MHD – stars: magnetic fields – stars: neutron – pulsars: general.

1 INTRODUCTION

Observations of low-field neutron stars in binary systems containing white-dwarf and supergiant companions, with a history of disc-fed and wind-fed accretion, respectively, suggest that the magnetic dipole moment $|\mathbf{m}|$ of a neutron star decreases monotonically with accreted mass, M_a (Taam & van den Heuvel 1986; van den Heuvel & Bitzaraki 1995; see Wijers 1997 for a dissenting view). Several mechanisms have been proposed to explain why $|\mathbf{m}|$ is reduced:

(i) accelerated ohmic decay, where the electrical conductivity of the crust is lowered by accretion-induced heating (Urpin & Geppert 1995; Urpin & Konenkov 1997);

(ii) interactions between superfluid neutron vortices and super-conducting magnetic fluxoids in the stellar interior (Muslimov & Tsygan 1985; Srinivasan et al. 1990); and

(iii) magnetic screening or burial, where the currents generating the natal magnetic field are partially neutralized by accretion-induced currents in the crust (Arons & Lea 1980; Blondin & Freese 1986).

For a critical review of these mechanisms, see Melatos & Phinney (2001).

In this paper, we study the mechanism of magnetic burial in detail. In the early stages of accretion ($M_a \lesssim 10^{-10}$ M$_\odot$), accreted matter accumulates in a column at the polar cap, minimally distorting the magnetic field. The mass–flux distribution in this regime has been calculated by Grad–Shafranov methods, with the prediction that $|\mathbf{m}|$ is reduced by ~ 1 per cent for $M_a \approx 10^{-10}$ M$_\odot$ (Hameury et al. 1983; Brown & Bildsten 1998; Litwin, Brown & Rosner 2001). We show that these calculations overestimate the amount of screening; in fact, $M_a \gtrsim 10^{-5}$ is required to reduce $|\mathbf{m}|$ by 10 per cent when the confining stress of the compressed, equatorial magnetic field is modelled faithfully. In this regime, inaccessible to previous analyses due to numerical breakdown (Hameury et al. 1983; Brown & Bildsten 1998; Litwin et al. 2001), the latitudinal pressure gradient at the base of the polar column forces the polar magnetic field to buckle, and the accreted material spreads equatorward together with frozen-in magnetic flux (Melatos & Phinney 2001). We compute the structure of the highly distorted magnetic field, and hence $|\mathbf{m}|$, as a function of M_a.

A key advance in the present work is that the mass–flux distribution in each equilibrium state is self-consistent; our equilibria are generated by a continuous deformation of the flux surfaces of the initial magnetic field (say, a dipole), in a manner which preserves flux-freezing. This is not true of previous calculations, where the mass–flux distribution is unconstrained relative to the initial state (Hameury et al. 1983; Brown & Bildsten 1998; Litwin et al. 2001; Melatos & Phinney 2001). However, several other important effects are not included to keep the problem manageable, as follows.

(i) Ohmic dissipation is neglected, even though the diffusion and accretion time-scales are comparable for the smallest magnetic structures predicted by the theory (Brown & Bildsten 1998; Cumming, Zweibel & Bildsten 2001).

[★]E-mail: d.payne@physics.unimelb.edu.au

(ii) We do not investigate the stability of the hydromagnetic equilibria we compute; sharp magnetic-field gradients are potentially disrupted by Rayleigh–Taylor and interchange instabilities (Bhattacharya 1999; Cumming et al. 2001; Melatos & Phinney 2001).

(iii) We treat the neutron star as a hard surface; subsidence of accreted material, and incorporation into the crust, are neglected (Bhattacharya 1999).

The paper is structured as follows. In Section 2, we introduce the theoretical framework for calculating the self-consistent hydromagnetic equilibrium state of an accreting neutron star. Analytic and numerical methods of solution are given in Section 3. The properties of the equilibria are investigated in Section 4, $|\boldsymbol{m}|$ is computed as a function of M_a and the radius of the polar cap, and the novel feature of magnetic bubbles is explored. The limitations of our results, with respect to time-dependent processes like hydromagnetic instabilities and ohmic dissipation, are assessed in Section 5.

2 THEORY OF EQUILIBRIA

2.1 Hydromagnetic force balance

The equations of non-ideal magnetohydrodynamics (MHD) in SI units (Bernstein, Frieman & Kruskal 1958) comprise the equation of mass conservation,

$$\frac{\partial \rho}{\partial t} + \nabla \cdot (\rho \boldsymbol{v}) = 0, \tag{1}$$

the equation of motion,

$$\rho \frac{\partial \boldsymbol{v}}{\partial t} + \rho (\boldsymbol{v} \cdot \nabla) \boldsymbol{v} = -\rho \nabla \phi - \nabla p + \frac{1}{\mu_0}(\nabla \times \boldsymbol{B}) \times \boldsymbol{B}, \tag{2}$$

and the induction equation (minus the displacement current),

$$\frac{\partial \boldsymbol{B}}{\partial t} - \nabla \times (\boldsymbol{v} \times \boldsymbol{B}) = \frac{1}{\mu_0 \sigma} \nabla^2 \boldsymbol{B}, \tag{3}$$

supplemented by $\nabla \cdot \boldsymbol{B} = 0$ and an adiabatic or isothermal equation of state, $d(p\rho^{-\Gamma})/dt = 0$. In this notation, $\boldsymbol{B}$, ρ, p, ϕ, $\boldsymbol{v}$ and σ represent the magnetic field, mass density, kinetic pressure, gravitational potential, plasma bulk velocity and electrical conductivity, respectively. Elastic stresses are neglected (Romani 1990; Melatos & Phinney 2001), as is the Hall effect (Geppert & Rheinhardt 2002).

In the magnetostatic limit, defined by $\boldsymbol{v} = \boldsymbol{0}$ and $\partial/\partial t = 0$, the equation of motion reduces to

$$\nabla p + \rho \nabla \phi - \frac{1}{\mu_0}(\nabla \times \boldsymbol{B}) \times \boldsymbol{B} = 0. \tag{4}$$

The local Alfvén time-scale, $\tau_A = L/v_A \lesssim 4 \times 10^{-2}$ s for ($L \lesssim 50$ m), is much shorter than the accretion time, $\tau_a \sim 10^7$ yr. Equations (1) and (3) are also satisfied identically (in the ideal-MHD limit $\sigma \to \infty$) and drop out of the problem. To preserve the information encoded in (1) and (3), we must impose an auxiliary constraint on the mass–flux distribution of the final state in order to connect it with the initial state and uniquely specify the problem. The constraint expresses the fact that material cannot flow across magnetic flux surfaces in the limit $\sigma \to \infty$. We delay consideration of ohmic dissipation, where magnetic flux diffuses through the fluid at short length-scales via (3), to a future paper.

We define spherical polar coordinates (r, θ, ϕ) such that $\theta = 0$ defines the symmetry axis of the pre-accretion magnetic field. For an axisymmetric configuration, there exists a scalar flux function $\psi(r, \theta)$ that generates $\boldsymbol{B}$ via

$$\boldsymbol{B} = \frac{\nabla \psi}{r \sin \theta} \times \hat{\boldsymbol{e}}_\phi. \tag{5}$$

The toroidal component B_ϕ is zero at all times, if the accretion process is axisymmetric and $B_\phi = 0$ in the initial accretion state. Upon substituting (5) into (4), we obtain

$$\nabla p + \rho \nabla \phi + (\Delta^2 \psi) \nabla \psi = 0, \tag{6}$$

with

$$\Delta^2 = \frac{1}{\mu_0 r^2 \sin^2 \theta} \left[\frac{\partial^2}{\partial r^2} + \frac{\sin \theta}{r^2} \frac{\partial}{\partial \theta} \left(\frac{1}{\sin \theta} \frac{\partial}{\partial \theta} \right) \right]. \tag{7}$$

We can then resolve (6) into components parallel and perpendicular to the magnetic field:

$$\rho \nabla \phi + \nabla p = 0, \tag{8}$$

$$\rho \nabla \phi + \nabla p + (\Delta^2 \psi) \nabla \psi = 0. \tag{9}$$

In this paper, we assume the accreted material forms an isothermal atmosphere, with $p = c_s^2 \rho$, where c_s denotes the isothermal sound speed. [The force equation for a general equation of state $p = p(\rho)$ is given in appendix A of Mouschovias (1974).] The gravitational potential ϕ, determined by Poisson's equation, $\nabla^2 \phi = 4\pi G \rho$, is the sum of contributions from the accreted material (M_a) and the underlying neutron star (M_*), with $M_a \ll M_*$. As the hydromagnetic length-scale $|\boldsymbol{B}|/|\nabla \boldsymbol{B}|$ is much smaller than the hydrostatic length-scale $|p|/|\rho \nabla \phi|$ (verified a posteriori), $\nabla \phi$ is approximately constant near the stellar surface for our purposes, i.e.

$$\phi = GM_* r/R_*^2, \tag{10}$$

where M_* and R_* are the mass and radius of the neutron star.

We use the method of characteristics to solve (6) assuming the gravitational field is radial ($M_a \ll M_*$). The r component reads $\rho_r + (\Delta^2 \psi)/c_s^2 \psi_r = -\rho/c_s^2 \phi_r$ and the θ component reads $\rho_\theta = (\Delta^2 \psi)/c_s^2 \psi_\theta$, where subscripts indicate differentiation. Together these become: $\rho_r + (\psi_r/\psi_\theta)\rho_\theta = -\rho/c_s^2 \phi_r$. The characteristic equation is: $dr = (\psi_\theta/\psi_r) d\theta = -d\rho/(\phi \rho)$. This is solved to yield the two characteristic curves: $\log \rho + \phi/c_s^2 = C_1$ and $\psi = C_2$. Thus the characteristic solution is $\log \rho + \phi/c_s^2 = f(\psi)$ or, equivalently,

$$p = F(\psi) \exp \left[-(\phi - \phi_0)/c_s^2 \right] \tag{11}$$

where $F(\psi) = \exp[f(\psi)]$ is an arbitrary positive function to be specified and $\phi_0 = GM_*/R_*$ is a reference potential. This is just the usual barometric formula with a different base pressure $F(\psi)$ for each field line. Note that ∇F is parallel to $\nabla \psi$, so ψ and hence F are constant along a field line, and one has $\nabla F = F'(\psi)\nabla \psi$. Substituting into (6), we obtain a second-order, non-linear, elliptic partial differential equation, the Grad–Shafranov equation, for ψ:

$$\Delta^2 \psi = -F'(\psi) \exp \left[-(\phi - \phi_0)/c_s^2 \right]. \tag{12}$$

Equation (12) can be understood as follows. The quantity F is a function of r and θ through ψ at hydrostatic equilibrium, expressing the fact that magnetic forces act only perpendicular to field lines, while pressure gradients balance gravity along field lines. If $\psi(r, \theta)$ is given, and if matter is distributed between field lines so that the forces parallel to field lines are in exact balance, then forces perpendicular to the field lines are brought into balance by the appropriate current density $\mu_0^{-1} \nabla \times \boldsymbol{B}$.

2.2 Magnetic flux-freezing and the mass–flux ratio

Many authors guess $F(\psi)$ when modelling various systems, e.g. structures in the solar corona, like prominences and arcades (Dungey 1953; Low 1980), and accreting compact objects (Uchida & Low

1981; Hameury et al. 1983; Brown & Bildsten 1998; Melatos & Phinney 2001). As $F(\psi)$ does not change in passing from the initial (pre-accretion) to the final (post-accretion) state in the ideal-MHD limit, the guessed $F(\psi)$ conflicts with the initial $F(\psi)$ except under very special circumstances. In this paper, we adopt a self-consistent approach whereby we calculate $F(\psi)$ explicitly by demanding that the mass–flux distribution of the final state equals that of the initial state, plus the accreted material, as described below.

Define a local coordinate system (s, t), with unit vectors $\hat{\boldsymbol{e}}_s = \boldsymbol{B}/|\boldsymbol{B}|$ and $\hat{\boldsymbol{e}}_t = \nabla\psi/|\nabla\psi|$ parallel and perpendicular to the magnetic field, respectively. The amount of matter between two infinitesimally separated flux surfaces ψ and $\psi + \mathrm{d}\psi$ is $\mathrm{d}M = 2\pi \int_C \mathrm{d}s\mathrm{d}t\, \rho r \sin\theta$, where $\mathrm{d}s\mathrm{d}t = |\hat{\boldsymbol{e}}_s\, \mathrm{d}s \times \hat{\boldsymbol{e}}_t\, \mathrm{d}t| = \mathrm{d}s\, \mathrm{d}\psi/|\nabla\psi|$ is an infinitesimal area element, and C is the curve $\psi[r(s), \theta(s)] = \psi$. Hence we can write

$$\frac{\mathrm{d}M}{\mathrm{d}\psi} = 2\pi \int_C \mathrm{d}s\, \rho[r(s), \theta(s)] r \sin\theta |\nabla\psi|^{-1}, \tag{13}$$

where $\mathrm{d}M/\mathrm{d}\psi$ is the mass–flux ratio. Upon substituting (11) into (13), we arrive at

$$F(\psi) = \frac{c_s^2}{2\pi} \frac{\mathrm{d}M}{\mathrm{d}\psi} \left\{ \int_C \mathrm{d}s\, r \sin\theta |\nabla\psi|^{-1} \mathrm{e}^{-(\phi-\phi_0)/c_s^2} \right\}^{-1}, \tag{14}$$

which is to be solved simultaneously with (12) for $\psi(r, \theta)$ given $\mathrm{d}M/\mathrm{d}\psi$. For problems involving accretion, the mass–flux constraint is not conservative; $\mathrm{d}M/\mathrm{d}\psi$ in the final state equals $\mathrm{d}M/\mathrm{d}\psi$ in the initial state plus the mass–flux distribution of the accreted material.

In disc-fed accretion, mass accretes on to polar magnetic field lines that close beyond the inner edge of the accretion disc, located at a radius

$$\frac{R_a}{R_*} \approx 270 \left(\frac{\dot{M}}{10^{-9}\, \mathrm{M_\odot\, yr^{-1}}} \right)^{-2/7} \left(\frac{|\boldsymbol{m}|}{10^{20}\, \mathrm{T\, m^3}} \right)^{4/7} \tag{15}$$

in the equatorial plane (Basko & Sunyaev 1976; Ghosh & Lamb 1979). The flux surface that closes at R_a is related to the flux surface at the stellar equator, $\psi_* = \psi(R_*, \pi/2)$, by $\psi_a = \psi_* R_*/R_a$, for a dipole. We do not model the mechanism by which plasma enters the magnetosphere (e.g. Rayleigh–Taylor and Kelvin–Helmholtz instabilities at $R \approx R_a$), which sets the form of $\mathrm{d}M/\mathrm{d}\psi$ in reality, as this is an unsolved problem (Basko & Sunyaev 1976; Arons et al. 1984). Instead, we assume that the accreted mass is distributed nearly uniformly within the polar flux tube $0 \leqslant \psi \leqslant \psi_a$, and that leakage on to flux surfaces $\psi_a \leqslant \psi \leqslant \psi_*$ is minimal. A step change in $\mathrm{d}M/\mathrm{d}\psi$ at ψ_a leads to numerical problems, so we approximate the mass distribution over one hemisphere by $M(\psi) = M_a(1 - \mathrm{e}^{-\psi/\psi_a})/2(1 - \mathrm{e}^{-\psi_*/\psi_a})$. We have checked that the solution of (12) and (14) is not sensitive to the exact functional form of $\mathrm{d}M/\mathrm{d}\psi$. Finally, we assume that the accreted material does not transport any magnetic flux, e.g. from the accretion disc (cf. Uchida & Low 1981). If the magnetic dipole moment is less than $\approx 10^{16}\, \mathrm{T\, m^3}$, we have $\psi_a \approx \psi_*$ (Cheng & Zhang 1998) and the above functional form of $M(\psi)$ is inadequate. This occurs at the latest stages of accretion ($M_a > 0.1\, \mathrm{M_\odot}$), outside the regime modelled in this paper.

2.3 Initial and boundary conditions

In this paper, we investigate the distortion of an initially dipolar magnetic field,

$$\psi_i(r, \theta) = \psi_* R_* r^{-1} \sin^2\theta, \tag{16}$$

with $\psi_* = B_* R_*^2/2$, where B_* is the polar magnetic field before accretion. Given $\mathrm{d}M/\mathrm{d}\psi$ as a function of M_a, we solve (12) and (14) subject to the Dirichlet boundary conditions

$$\psi(R_*, \theta) = \psi_* \sin^2\theta \quad \text{and} \quad \lim_{r \to \infty} \psi(r, \theta) = 0. \tag{17}$$

At the surface, i.e. the crystalline layers of density $\lesssim 4 \times 10^{14}\, \mathrm{kg\, m^{-3}}$, the field is dipolar. Far from the star, one has $\psi \propto r^{-1}$, as for any localized, static current distribution. The approximation that the surface field remains dipolar at all times is valid provided that M_a is small compared to M_*, for then the footpoints of the magnetic field lines are anchored to the highly conducting, high-inertia interior of the star. The surface field may be generated deep in the neutron-star core or by a dynamo in the inner crust (Thompson & Duncan 1993; Konenkov & Geppert 2001). This line-tying boundary condition is a feature of models of magnetic loops in the solar corona (Low 1980; Zweibel & Hundhausen 1982) and earlier work on neutron-star accretion (Uchida & Low 1981; Hameury et al. 1983; Brown & Bildsten 1998; Litwin et al. 2001). A drawback of preventing the accreted matter from sinking is that unrealistically high densities ($\geqslant 4 \times 10^{14}\, \mathrm{kg\, m^{-3}}$) are produced locally, at the base of the column, for $M_a > 10^{-8}\, \mathrm{M_\odot}$. Recent modelling of the magnetic field beneath the surface of an accreting neutron star, based on (3) with a velocity distribution for the superfluid assumed, illustrates the effects of submergence and subsequent incorporation of accreted matter into the crust (Choudhuri & Konar 2002). Cumming (2002) discusses a vacuum (like in this paper) and a screened boundary condition at the surface.

In the numerical calculations presented in Section 4, two extra grid-related boundaries are introduced: the outer radius of the grid, at $r = R_m$, and the lines $\theta = 0$ and $\theta = \pm \pi/2$, arising when the grid is restricted to one quadrant or hemisphere. We choose R_m large enough to include the layer where the accretion-induced screening currents lie, i.e., above the greater of the hydrostatic (c_s^2/g) and Alfvén ($|\boldsymbol{B}|/|\nabla\boldsymbol{B}|$) scaleheights. In practice, this is achieved by increasing R_m until the dipole moment of the solution varies by less than 0.1 per cent. At $r = R_m$, the magnetic field is taken to be radial, with $\partial\psi/\partial r(R_m, \theta) = 0$, i.e. a free boundary. [It is outside the scope of this paper to model the disc–magnetosphere interface in detail; see Rastätter & Schindler (1999).] Another possible way to treat the boundary condition at $r = R_m$ is to set $\psi(R_m, \theta) = \psi_m \sin^2\theta$ and adjust ψ_m iteratively to give the self-consistent dipole moment of the solution, but we encountered numerical difficulties with this approach.

There are two physically plausible choices for the polar and equatorial boundary conditions: (i) $\psi(r, \pi) = 0$ and $\partial\psi/\partial\theta(r, \pi/2) = 0$, as for the initial dipole, or (ii) $\partial\psi/\partial\theta(r, \pm \pi/2) = 0$, north–south symmetry. We mostly adopt (i) but explore (ii) for completeness in Section 4.6, where it is shown that field lines on either side of the pole are peeled away, leaving the $\psi = 0$ line isolated, without affecting the dipole moment significantly. Strictly speaking, the conditions $\partial\psi/\partial\theta(r, \pi/2) = 0$ and $\partial\psi/\partial r(R_m, \pi/2) = 0$ force the magnetic field to vanish artificially at $(R_m, \pi/2)$, but $|\boldsymbol{m}|$ is affected by less than 0.1 per cent (see Section 4).

3 SOLUTION METHODS

In this section, we discuss three ways to solve (12) and (14): analytically by Green functions (Section 3.1), analytically in the small-M_a approximation (Section 3.2), and numerically, by an iterative algorithm due to Mouschovias (1974) (Sections 3.3 and 3.4).

3.1 Green functions

The Grad–Shafranov boundary value problem (12),

$$\Delta^2 \psi(r, \theta) = Q(r, \theta), \tag{18}$$

with

$$\psi(R_*, \theta) = \psi_* \sin^2 \theta \quad \text{and} \quad \lim_{r \to \infty} \psi(r, \theta) = 0w, \tag{19}$$

can be solved analytically by Green functions if the source term $Q(r, \theta)$ is known as a function of r and θ. In principle, $Q(r, \theta)$ is given by (12) and (14); in practice, it is not known analytically. With ψ specified on the boundary S of the volume V, we can write (see Appendix A1)

$$\psi(\boldsymbol{x}) = \int_V \mathrm{d}^3 x' G^* Q + \int_S \mathrm{d}^2 x' (\psi \nabla G^* - G^* \nabla \psi + \boldsymbol{b} \psi G^*), \tag{20}$$

where G and G^* are Green functions for $L = \mu_0 \, r^2 \, \sin^2 \theta \nabla^2$ and its adjoint L^*, satisfying

$$\frac{\partial^2 G}{\partial r^2} + \frac{(1 - \mu^2)}{r^2} \frac{\partial^2 G}{\partial \mu^2} = \frac{1}{r^2} \delta(r - r') \delta(\mu - \mu'), \tag{21}$$

and

$$\frac{\partial^2 G^*}{\partial r^2} + \frac{(1 - \mu^2)}{r^2} \frac{\partial^2 G^*}{\partial \mu^2} + \frac{4}{r} \frac{\partial G^*}{\partial r} - \frac{4\mu}{r^2} \frac{\partial G^*}{\partial \mu}$$
$$= \frac{1}{r^2} \delta(r - r') \delta(\mu - \mu'), \tag{22}$$

with $\mu = \cos \theta$ and $\boldsymbol{b} = -2r^{-1}(\hat{\boldsymbol{e}}_r + \cot \theta \hat{\boldsymbol{e}}_\theta)$. Upon solving (21) and (22), we obtain

$$G(r, \mu, r', \mu') = \sum_{\ell=0}^{\infty} N_\ell^{-1} g_{\ell+1}(r, r')(1 - \mu^2) C_\ell^{3/2}(\mu') C_\ell^{3/2}(\mu), \tag{23}$$

and

$$G^*(r, \mu, r', \mu') = \sum_{\ell=0}^{\infty} N_\ell^{-1} g_\ell^*(r, r')(1 - \mu'^2) C_\ell^{3/2}(\mu') C_\ell^{3/2}(\mu), \tag{24}$$

with

$$g_\ell(r, r') = \frac{1}{(2\ell + 1)r'^2} \frac{r_<^{\ell+1}}{r_>^\ell} \left[\left(\frac{R_*}{r_<} \right)^{2\ell+1} - 1 \right], \tag{25}$$

$$r_< = \min(r, r'), \quad r_> = \max(r, r'),$$

$$g_\ell^*(r, r') = \left(\frac{r'}{r} \right)^2 g_{\ell+1}(r, r'), \tag{26}$$

$$N_\ell = 2(\ell + 1)(\ell + 2)(2\ell + 3)^{-1}, \tag{27}$$

and hence, from (20), we arrive at the complete solution

$$\psi(r, \mu) = \frac{\psi_* R_*(1 - \mu^2)}{r} + (1 - \mu^2) \sum_{\ell=0}^{\infty} N_\ell^{-1} C_\ell^{3/2}(\mu)$$
$$\times \int_{-1}^{1} \mathrm{d}\mu' \int_{R_*}^{\infty} \mathrm{d}r' r'^2 g_\ell^*(r', r) C_\ell^{3/2}(\mu') Q(r', \mu'). \tag{28}$$

$C_\ell^{3/2}(\mu)$ denotes a Gegenbauer polynomial of order ℓ (see Appendix A).

3.2 Analytic approximation for small M_a

In the limit of small M_a, where $\mathrm{d}M/\mathrm{d}\psi$ and hence $Q(r, \theta)$ are small, one can show (see Appendix A3) that the magnetic flux distribution reduces to

$$\psi(r, \theta) = \psi_i(r, \theta)(1 - b^2 M_a/M_c) \tag{29}$$

far from the star ($r \to \infty$), with

$$M_c = 2\pi G M_* \psi_*^2 / \mu_0 c_s^4 R_*^2 \tag{30}$$

For convenience, we write this using CGS units

$$\frac{M_c}{M_\odot} = 1.2 \times 10^{-4} \left(\frac{c_s}{10^8 \, \mathrm{cm \, s^{-1}}} \right)^{-4} \left(\frac{B_*}{10^{12} \, \mathrm{G}} \right)^2, \tag{31}$$

where $M_* = 1.4 \, M_\odot$ and $R_* = 10^6$ cm.

It follows that the magnetic dipole moment scales as $|\boldsymbol{m}| = |\boldsymbol{m}_i|(1 - M_a/M_c)$. This scaling agrees, in the small-M_a limit, with empirical scalings of the form $|\boldsymbol{m}| = |\boldsymbol{m}_i|(1 + M_a/M_c)^{-1}$, with $M_c \approx 10^{-5} \, M_\odot$, that have been proposed in the literature (Shibazaki et al. 1989; Cheng & Zhang 1998).

3.3 Iterative numerical scheme

To solve (12) and (14) self-consistently for $\psi(r, \theta)$ for $M_a \gg M_c$, we employ an iterative numerical algorithm similar to the one introduced by Mouschovias (1974) to study the Parker instability of the Galactic magnetic field. The algorithm and its performance are discussed in detail in Appendices A and B and summarized briefly here.

Given $\mathrm{d}M/\mathrm{d}\psi$ and an initial guess $\psi^{(0)}(r, \theta)$, we calculate the locations of N_c contours of ψ, spaced either linearly or logarithmically in ψ, capturing topologically disconnected contours and closed loops (Snyder 1978). We then compute $F[\psi^{(0)}]$ from (14) and hence $F'[\psi^{(0)}]$ after polynomial fitting (simple differencing causes numerical difficulties; see Appendix B3). The Poisson equation (12) is solved with this source term using successive overrelaxation to obtain $\psi_{new}^{(0)}(r, \theta)$, and the next iterate is obtained by underrelaxation: $\psi^{(n+1)} = \Theta^{(n)} \psi^{(n)} + [1 - \Theta^{(n)}] \psi_{new}^{(n)}$, with $0 \leqslant \Theta^{(n)} \leqslant 1$. Iteration continues until the convergence criterion $|\psi_{new}^{(n+1)} - \psi^{(n)}| < \epsilon |\psi_{new}^{(n+1)}|$ is satisfied on average across the grid. We usually take $\epsilon = 10^{-2}$ in this paper. Physically, the algorithm starts from a trial magnetic field (and associated current distribution), the accreted mass M_a is distributed among the flux tubes according to $\mathrm{d}M/\mathrm{d}\psi$, mass is allowed to slide up or down flux tubes to achieve hydrostatic equilibrium along $\boldsymbol{B}$, a new current distribution is computed that balances forces perpendicular to $\boldsymbol{B}$, and the process is repeated.

3.4 Numerical convergence

There is no general rule for choosing $\Theta^{(n)}$. We find, by experimentation, that one must decrease $1 - \Theta^{(n)}$ as M_a increases; a useful rule of thumb is

$$1 - \Theta^{(n)} \approx (M_a/10^{-7} M_\odot)^{-1} (\psi_*/10\psi_a)^{-2},$$

for $M_a \geqslant 10^{-7} \, M_\odot$. More details can be found in Table B1 and Appendix B4. At least $2/[(1 - \Theta) \log_{10}(\epsilon)]$ iterations are required for convergence; bootstrapping is recommended, i.e. using the equilibrium solution for a lower value of M_a as the first iterate instead of the dipole. We show in Appendix B5 that the error in ψ averaged over the grid scales as $G^{-1.6}$, where G is the number of grid cells in each dimension. The optimum number of contours is $N_c \approx G - 1$; $F'(\psi)$ becomes jagged for $N_c \gg G$ due to grid crossings

Figure 1. Mean residual versus iteration number. $M_a = 10^{-6} \, M_\odot$, $\theta = 0.995$ (top). $M_a = 10^{-5} \, M_\odot$, $\theta = 0.95$ (bottom).

Figure 2. Polar plot of equilibrium magnetic field lines (solid curves) and density contours (dashed curves) for $M_a = 10^{-5} \, M_\odot$. The coordinates measure altitude above the stellar surface. Density contours are drawn for $\eta \rho_{max}$ (maximum at the pole, $\rho_{max} = 2.52 \times 10^{17} \, \text{kg m}^{-3}$) with $\eta = 0.8, 0.6, 0.4, 0.2, 0.01, 0.001, 10^{-4}, 10^{-5}, 10^{-6}, 10^{-12}$.

10^8 T (Hartman et al. 1997), $c_s = 10^6 \, \text{m s}^{-1}$, $x_0 = c_s^2 R_*^2 / GM_* = 0.54$ m and hence $a = R_*/x_0 = 1.86 \times 10^4$ (Brown & Bildsten 1998). The results are mostly presented in rectangular (r, θ) plots scaled logarithmically where appropriate to emphasize the boundary layer of compressed magnetic field.

4.1 Structure of the polar mountain and equatorial magnetic tutu

During the early stages of accretion, matter piles up on the polar cap, confined by the tension of the polar magnetic flux tube. However, for $M_a \gtrsim 10^{-5} \, M_\odot$, the hydrostatic pressure at the base of the accretion column overcomes the magnetic tension and matter spreads over the stellar surface towards the equator, dragging along frozen-in polar field lines. The spreading distorts $\boldsymbol{B}$, generating screening currents $\mu_0^{-1} \nabla \times \boldsymbol{B}$, which act to decrease the magnetic dipole moment ($|\boldsymbol{m}|$ is dominated by the polar field). In its turn, the spreading is also counteracted by the tension of the magnetic field lines compressed towards the equator. These equatorial stresses, neglected in previous work (Hameury et al. 1983; Brown & Bildsten 1998; Litwin et al. 2001), greatly increase the M_a required to reduce $|\boldsymbol{m}|$.

Fig. 2 shows the magnetic field configuration and density profile for $M_a = 10^{-5} \, M_\odot$ in cross-section (cf. schematic version in Fig. 1 of Melatos & Phinney 2001). The 'polar mountain' of accreted material is readily apparent, traced out by the dashed contours. Fig. 3 shows the distorted magnetic field configuration overlaid on the field lines of the undisturbed dipole. The distorted field exhibits a pinched, flaring geometry, termed an 'equatorial tutu' by Melatos & Phinney (2001). A more complete view of the overall hydromagnetic structure can be gained from Fig. 4. The tutu-like field is shown again in Figs 4(a) and (b), while the polar mountain (ρ) is shown in Fig. 4(c). In Fig. 4(d), where the radius of curvature of $\boldsymbol{B}$ is smaller than the hydrostatic scaleheight x_0, the toroidal screening currents are confined below altitude x_0, and are concentrated near the polar cap. (Note that ohmic dissipation, neglected here, is important at these scales.) The $\boldsymbol{J} \times \boldsymbol{B}$ force per unit volume (Fig. 4e) balances the pressure gradient (Fig. 4f), preventing the accreted material from spreading all the way to the equator.

(as demonstrated in Fig. B1 in Appendix B). To concentrate maximum grid resolution near the stellar surface and at the edge of the polar cap ($\psi = \psi_a$), where screening currents predominantly reside and gradients of ρ and ψ are steepest, we scale the r and θ coordinates logarithmically as described in Appendix B1.

Fig. 1 displays the mean residual as a function of iteration number. Convergence is rapid for $M_a \leqslant 10^{-6} \, M_\odot$ and poor for $M_a \geqslant 10^{-4} \, M_\odot$. Large fluctuations in the mean residual are mainly due to the polynomial fit to $F(\psi)$ and the appearance of magnetic bubbles (see Section 4.7).

4 EQUATORWARD HYDROMAGNETIC SPREADING

In this section, we present the results of the analytic and numerical calculations described in Section 3. The hydromagnetic structure of the polar 'mountain' formed by the accreted material is described in Sections 4.1 and 4.3 and compared with previous calculations in which $F(\psi)$ is arbitrary (e.g. Brown & Bildsten 1998). The physics of equatorward spreading of the accreted material and the formation of an equatorial magnetic 'tutu', including a criterion for the onset of spreading, is discussed in Section 4.4. The scalings of $|\boldsymbol{m}|$ with respect to M_a and $b = \psi_*/\psi_a$ are derived analytically and numerically in Sections 4.5 and 4.6. Finally, the formation of magnetic bubbles disconnected from the star – a new effect – is explored in Section 4.7. We start from the undisturbed dipole (16) and adopt the following physical parameters: $M_* = 1.4 \, M_\odot$, $R_* = 10^4$ m, $B_* =$

Figure 3. Polar plot of magnetic field lines after accretion (solid curves) and before accretion (dashed curves) for $M_a = 10^{-5}$ M$_\odot$. The coordinates measure altitude above the stellar surface.

The maximum density, attained at $(r, \theta) = (R_*, 0)$, is found empirically to be $\rho_{max} = M_a b^2/(2x_0^3 \pi \ a^2) \approx 6 \times 10^{12} (b/10)^2$ $(M_a/10^{-10} $ M$_\odot)$ kg m^{-3}, in accord with analytic estimates for $\rho(r, \theta) \approx \rho_{max} \exp(-x/x_0) \exp(-\psi/\psi_a)$ carried out in Appendix A. Consequently, ρ_{max} exceeds the crustal density 4×10^{14} kg m^{-3} for $M_a \geqslant 10^{-8}$ M$_\odot$. In reality, this overdensity is moderated by sinking (Brown & Bildsten 1998; Choudhuri & Konar 2002), which is prevented by the hard surface in our calculation. (We can alleviate the overdensity in our model by relaxing the isothermal assumption or allowing a non-barometric density distribution along contours.) For $M_a \geqslant 10^{-6}$ M$_\odot$, the maximum magnetic field strength becomes unrealistically large ($B_{max} \gtrsim 10^{11}$ T) below an altitude x_0, in response to ρ_{max}. Such field strengths formally exceed the yield stress of the crust (Romani 1990).

4.2 Sinking

The proportion of the accreted material that sinks is not well constrained. We consider a crude model of sinking in which a proportion s of the accreted matter sinks, leaving a proportion $(1 - s)$ to spread. This is modelled by setting

$$\frac{dM}{d\psi} = \frac{M_a}{\psi_a} \left[\frac{(1-s)e^{-\psi/\psi_a}}{2(1 - e^{-\psi_*})} + \frac{s}{2b} \right]. \tag{32}$$

We find that for $M_a = 10^{-5}$ M$_\odot$, and for $s = 0.9$ (i.e. all but 10^{-6} M$_\odot$ redistributed), the resultant dipole moment increases from ≈ 0.91 to 0.96.

4.3 Self-consistent mass–flux distribution

In previous studies of neutron-star accretion, $F(\psi)$ was chosen arbitrarily (Uchida & Low 1981; Hameury et al. 1983; Brown & Bildsten 1998; Litwin et al. 2001; Melatos & Phinney 2001). In this paper, by contrast, we determine $F(\psi)$ self-consistently by solving (12) and (14) simultaneously for a physically plausible choice of $dM/d\psi$ that places most of the accreted material at the poles of the initial, undisturbed dipole. Figs 5(a) and (b) compare our self-consistent $F(\psi)$ against the functional forms guessed by previous authors for two values of M_a. The differences are significant, especially near the pole ($\psi \approx 0$). [An analogous difference was discovered by Mouschovias

(1974) when solving for the final states of the Parker instability in the Galaxy self-consistently, relative to the previous guess of Parker (1966).] A polynomial fit in the numerical code yields the approximate form

$$F(\tilde{\psi}) = \exp(\tilde{\psi})(0.027\tilde{\psi}^4 - 0.13\tilde{\psi}^3$$
$$+ 0.21\tilde{\psi}^2 - 0.021\tilde{\psi} + 0.1333) \tag{33}$$

for $N_p = 4$, $M_a = 1.5 \times 10^{-4}$M$_\odot$, $b = 3$, $\tilde{\psi} = \psi/\psi_a$, and the choice of $dM/d\psi$ in Section 2.2.

4.4 Onset of spreading

Brown & Bildsten (1998) showed that, for an initially vertical field and neglecting the stress from compressed equatorial flux, the condition for spreading is given by $\alpha = B^2/2\mu_0 p \leqslant x_0/R_{cap} \approx 0.01$, where $R_{cap} = (R_*^3/R_a)^{1/2}$ is the polar cap radius. Given that $\alpha_{min} = B_*^2/(2\mu_0 p_{max}) \approx 0.27(B_*/10^8 $ T$)^2(M_a/10^{-12} $ M$_\odot)^{-1}$, it follows that the accreted matter distorts the magnetic field negligibly for $M_a \lesssim 3.7 \times 10^{-9}$ M$_\odot$ (i.e. $\alpha_{min} \gtrsim 0.01$). Above this value, progressively more distortion takes place for $M_a = 10^{-9}, 10^{-7}, 10^{-5}$ M$_\odot$, as shown in Fig. 6. The curved field lines have a large tangential component, previously negligible, which increases the magnetic field strength $|B|$ substantially for $M_a \gtrsim M_c/a = 8 \times 10^{-11}$ M$_\odot$, as predicted by the Green function analysis in Appendix A3. This induced magnetic pressure balances the overpressure of the accreted material. However, the effect on the magnetic dipole moment is negligible (<1 per cent) due to countervailing magnetic stresses from the compressed field at the equator; the magnetic radius of curvature is less than x_0 until M_a exceeds $\approx 1.4 \times 10^{-6}$ M$_\odot$, as proved in Appendix A3. Note that the compression of field lines as $|B|$ increases is imperceptible in Fig. 6 because of the extent of the horizontal axis; $|B|$ increases predominantly due to the B_θ component. The top of the boundary layer is roughly where B_θ vanishes, i.e. at an altitude $x = x_0 \ln [(a + 1)/(1 - M_c/M_a)] \approx 5.3$ m. for $M_a < M_c$.

We zoom in on the pole to compare with Litwin et al. (2001) in Fig. 7. Our results differ because Litwin et al. (2001) has a free boundary at the polar cap edge and ignores the θ terms in the Grad–Shafranov equation, while we impose north–south symmetry at the equator, with no condition at the polar cap edge. This allows the compressed magnetic field equatorward of the polar cap to push back on the polar flux tube. Furthermore, we prescribe $dM/d\psi$ and calculate $F(\psi)$ instead of prescribing $F(\psi)$. We observe curvature comparable to Litwin et al. (2001) for $M_a \approx 10^{-8}$ M$_\odot$ and thus the ballooning instability may be relevant, but a detailed calculation is beyond the scope of this paper.

An order-of-magnitude estimate of M_c, the mass required to buckle the magnetic field, can be obtained in the following way. The hydrostatic pressure at the base of the accreted column is given by $p_{max} = c_s^2 \rho_{max} = c_s^2 M_a b^2/(2\pi R_*^2 x_0)$, i.e. the weight per unit area of the mass M_a spread over approximately two hemispheres. This pressure is balanced by the tension of the magnetic field compressed into a layer of width $L \approx 6$ m along the surface and at the equator (see Fig. 2). In the layer, we have $B_1 \approx B_* R_*/L \approx 10^{12}$ T by flux conservation. Hence the hydrostatic and magnetic pressures balance for $M_a = 2B_*^2 R_*^4 yx_0/(c_s^2 \mu_0 L^2) \approx 2 \times 10^{-6}$ M$_\odot$ in accord with the numerical results.

4.5 Reduction of the magnetic dipole moment

The magnetic dipole moment

$$|\boldsymbol{m}| = \frac{3r^3}{4} \int_{-1}^{1} d(\cos\theta) \cos\theta B_r(r, \theta) \tag{34}$$
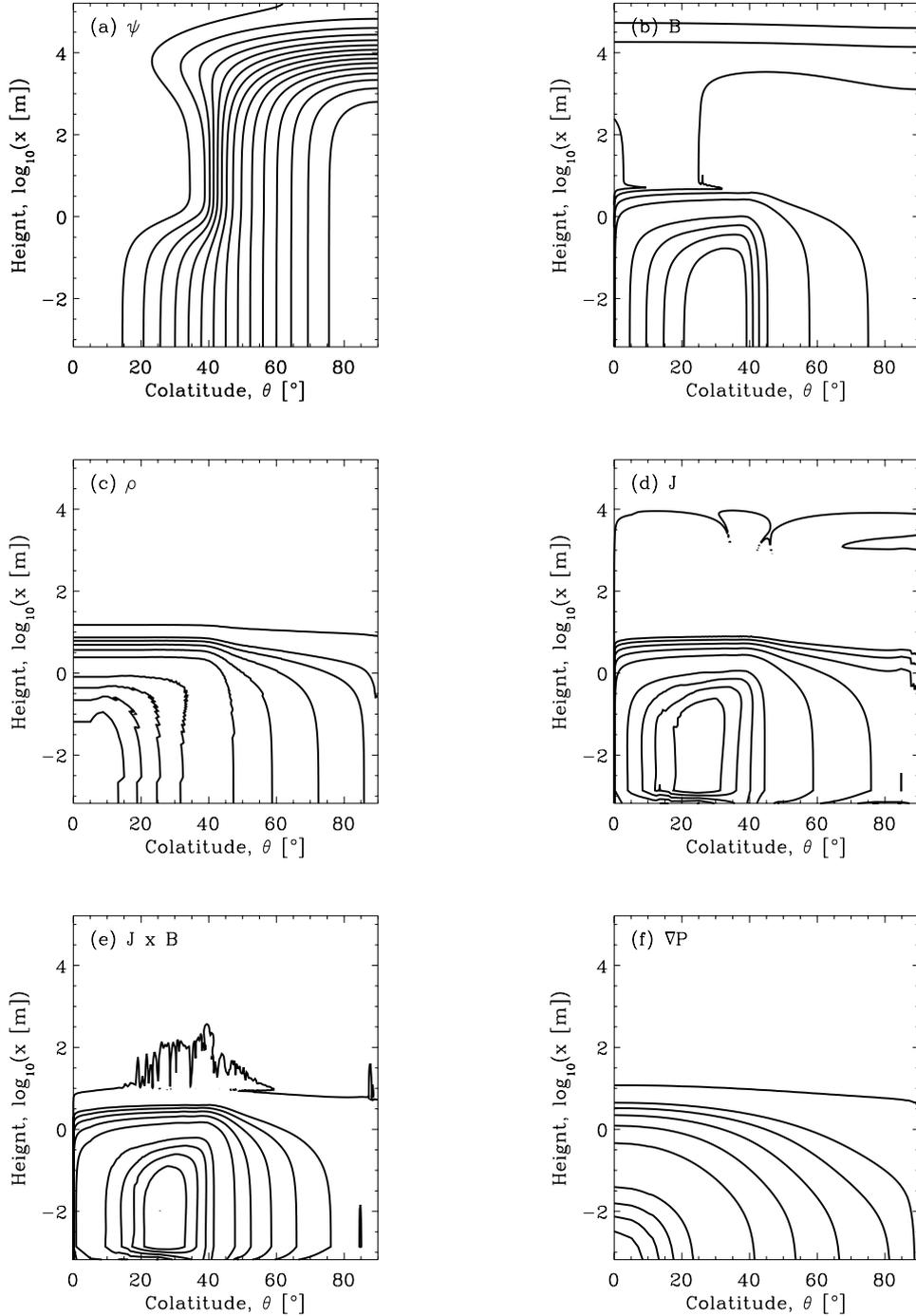
Figure 4. $M_a = 10^{-5}$ M$_\odot$. (a) Magnetic field lines (ψ contours), (b) magnetic field strength ($|\boldsymbol{B}|$ contours), (c) density, (d) current, (e) Lorentz force, and (f) pressure gradients. For each quantity x, values ηx_{max} are plotted, with $\eta = 0.8, 0.6, 0.4, 0.2, 0.01, 0.001, 10^{-4}, 10^{-5}, 10^{-6}, 10^{-12}$. Maximum values are found to be $\rho_{max} = 1.7 \times 10^{17}$ kg m^{-3}, $|\boldsymbol{B}|_{max} = 3.9 \times 10^{11}$ T, $|\boldsymbol{J}|_{max} = 2.0 \times 10^{15}$ A m^{-2}, $|\boldsymbol{J} \times \boldsymbol{B}|_{max} = 3.3 \times 10^{24}$ N m^{-3}, $|\nabla P|_{max} = 1.9 \times 10^{28}$ N m^{-3}.

is plotted as a function of r in Fig. 8(a). The screening currents are confined to a thin layer above the stellar surface; $|\boldsymbol{m}|$ is essentially constant with r above this layer. The layer is compressed as M_a increases, with half-width comparable to x_0 for $M_a \approx 10^{-4}$ M$_\odot$. The asymptotic value of $|\boldsymbol{m}|$ also decreases as M_a increases, as expected; equatorward hydromagnetic spreading drags magnetic flux away from the pole, and $|\boldsymbol{m}|$ is sensitive to B_r near the pole through (34).

Fig. 8(b) is a plot of $|\boldsymbol{m}|$ versus M_a. For $M_a \lesssim M_c = 1.2 \times 10^{-6}$ M$_\odot$, $|\boldsymbol{m}|$ decreases proportional to $(1 - M_a/M_c)$, as predicted

analytically in Section 3.2. For $M_a \gtrsim M_c$, we obtain the empirical relation

$$\frac{|\boldsymbol{m}|}{|\boldsymbol{m}_i|} = \left(\frac{M_a}{4.6 \times 10^{-5} \, \text{M}_\odot} \right)^{-2.25 \pm 0.22} \qquad (35)$$

by fitting a power law to the numerical results for $M_a \geqslant 5 \times 10^{-5}$ M$_\odot$, as in Fig. 8(c). However, (35) cannot be extrapolated reliably to the regime $M_a \gtrsim 10^{-4}$ M$_\odot$ for two reasons. First, our
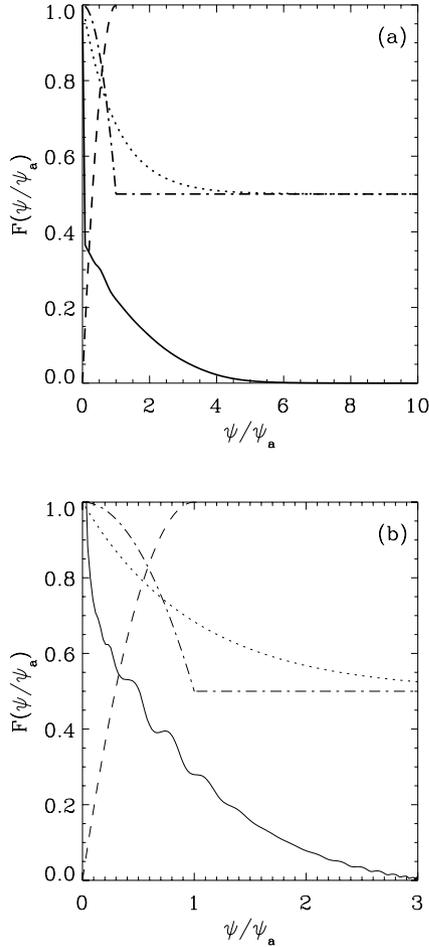
Figure 5. Comparison of the self-consistent $F(\psi)$ (solid) for (a) $M_a = 2 \times 10^{-5}\,\mathrm{M}_\odot$, $b = 10$ and (b) $M_a = 1.5 \times 10^{-4}\,\mathrm{M}_\odot$, $b = 3$ with others in the literature: Brown & Bildsten (1998) (dotted) Litwin et al. (2001) (dot-dashed), and Melatos & Phinney (2001) (dashed). These curves are scaled to the value at the pole, $F(0)$.

numerical scheme is limited by the steepness of gradients in the source term of (12). Physically, these scale as the hydrostatic pressure, with $\mathrm{d}F/\mathrm{d}\psi \propto M_a b$ as shown in Appendix A. We encounter convergence errors above 50 per cent for $M_a b \gtrsim 3 \times 10^{-4}\,\mathrm{M}_\odot$. Second, it is shown in Section 4.7 that magnetic bubbles, disconnected from the stellar surface, are created for $M_a b \gtrsim 10^{-4}\,\mathrm{M}_\odot$, leading to the steep dependence of $|\boldsymbol{m}|$ on M_a in (35). A word of caution: when bubbles appear, it is unclear how to interpret $|\boldsymbol{m}| = |\boldsymbol{m}|_{\mathrm{star}} + |\boldsymbol{m}|_{\mathrm{bubble}}$. In reality, one has $|\boldsymbol{m}|_{\mathrm{bubble}} = 0$ as $r \to \infty$, because the flux surfaces of the bubble are closed. However, at $= R_m$, the ingoing and outgoing flux tubes of the bubble do not cancel perfectly and one finds $|\boldsymbol{m}|_{\mathrm{bubble}} \neq 0$; bubble-related currents outside the solution domain ($r > R_m$), need to be included in order to recover $|\boldsymbol{m}|_{\mathrm{bubble}} = 0$.

4.6 Polar cap radius

We now discuss the effect on $|\boldsymbol{m}|$ of varying $b = \psi_a/\psi_*$, or equivalently the polar cap radius $R_{\mathrm{cap}} = R_* \sin^{-1}(b^{-1/2})$. Although R_{cap} is not known exactly without a detailed model of the flow of matter from the accretion disc to the stellar surface (Arons et al. 1984), estimates of its size from (15) are typically of order 1 km (Litwin

et al. 2001), i.e. $b \geqslant 100$, for $B_* = 10^8\,\mathrm{T}$ (Arons et al. 1984). Fig. 9 illustrates the magnetic configuration obtained for $b = 3$ and $= 10$, and $|\boldsymbol{m}|/|\boldsymbol{m}_i|$ is plotted versus M_a in Fig. 8(b), denoting $b = 3$ by crosses and $b = 10$ by triangles. Note how the equilibrium state changes with b. The mass–flux distribution $\mathrm{d}M/\mathrm{d}\psi \propto \exp(-\psi/\psi_a)$ implies a surface pressure distribution $F(\psi) \propto b \exp(-\psi/\psi_a)$, so larger b means steeper pressure gradients. (Numerical difficulties set in for $b = 30$, which can be partly alleviated by stretching the coordinates around ψ_a.) Importantly, however, we find M_c and the dipole moment $|\boldsymbol{m}|$ are independent of b. This is supported by the Green function analysis in Appendix A, except when $\mathrm{d}M/\mathrm{d}\psi$ depends explicitly on b, e.g. $\mathrm{d}M/\mathrm{d}\psi \propto b(1 - \psi/b\psi_a)^{1/2}$ implies $|\boldsymbol{m}| \propto b^{-1}$.

A related issue is whether $|\boldsymbol{m}|$ is affected in an unrealistic way by the boundary condition $\psi = 0$ at $\theta = 0$ in the examples presented so far. It is conceivable, for example, that the $\psi = 0$ line is unstable ('on a knife edge'), while neighbouring field lines are peeled away by accretion, unless it is forced to remain rectilinear artificially. As it happens, however, this is not the case. Fig. 10 shows the output of an experiment where the grid extends from equator to equator ($|\theta| < \pi/2$), and no boundary condition is imposed at $\theta = 0$. Clearly, the magnetic field and density profiles remain symmetric about the magnetic pole, with $\psi = 0$ at $\theta = 0$ emerging naturally, while $|\boldsymbol{m}|$ is essentially unchanged.

4.7 Buoyant magnetic bubbles

From the sequence of panels in Fig. 6 ($M_a/\mathrm{M}_\odot = 10^{-9}, 10^{-7}, 10^{-5}$), we observe that the magnetic field becomes increasingly distorted as M_a increases. Eventually, for $M_a \gtrsim 10^{-5}\,\mathrm{M}_\odot$, closed magnetic bubbles are created that are disconnected topologically from the surface of the star. This phenomenon is illustrated in Fig. 11. At the value of M_a where a bubble is first created, a magnetic neutral point (Y point) is observed to form on a field line near, but not at the pole. The bubble closes at $r < R_m$ in our simulation, but this may be a result of the approximate free boundary condition $\partial\psi/\partial\theta(R_m, \theta) = 0$; in reality, it may connect to the accretion disc.

Bubbles correspond to a loss of equilibrium, analogous to that which occurs during eruptive solar phenomena (Klimchuk & Sturrock 1989), where no simply connected hydromagnetic equilibrium exists. In the Grad–Shafranov boundary problem, the source term $\propto F'(\psi)$ in (12) increases with $M_a b$, boosting $\Delta^2\psi$ and hence ψ above the surface (to balance the weight of the added material through the Lorentz force). Above a critical value of M_a, flux surfaces are created with $\psi < 0$ or $\psi > \psi_*$, which are disconnected from the star and either form closed loops or are anchored 'at infinity' (here the accretion disc). This is shown explicitly by (A19) in the special case $F'(\psi) = $ constant. From our numerical results, we conclude that the critical M_a for bubble creation satisfies

$$M_a \geqslant 10^{-4} b^{-1}\,\mathrm{M}_\odot. \tag{36}$$

Note that bubble creation is a topological imperative. It is not the result of a hydromagnetic instability, e.g. interchange or Rayleigh–Taylor (Bernstein et al. 1958; Parker 1966; Mouschovias 1974).

Are the bubbles merely numerical artefacts (Brown & Bildsten 1998)? No. Equation (A19) demonstrates explicitly that flux surfaces with $\psi < 0$ or $\psi > \psi_*$ are created for M_a satisfying (36), at least for $F'(\psi) = $ constant. A more subtle issue is whether bubbles are the by-product of an artificial assumption in our idealized calculation. For example, if submergence of accreted material were permitted, it might reduce the pressure gradients that produce
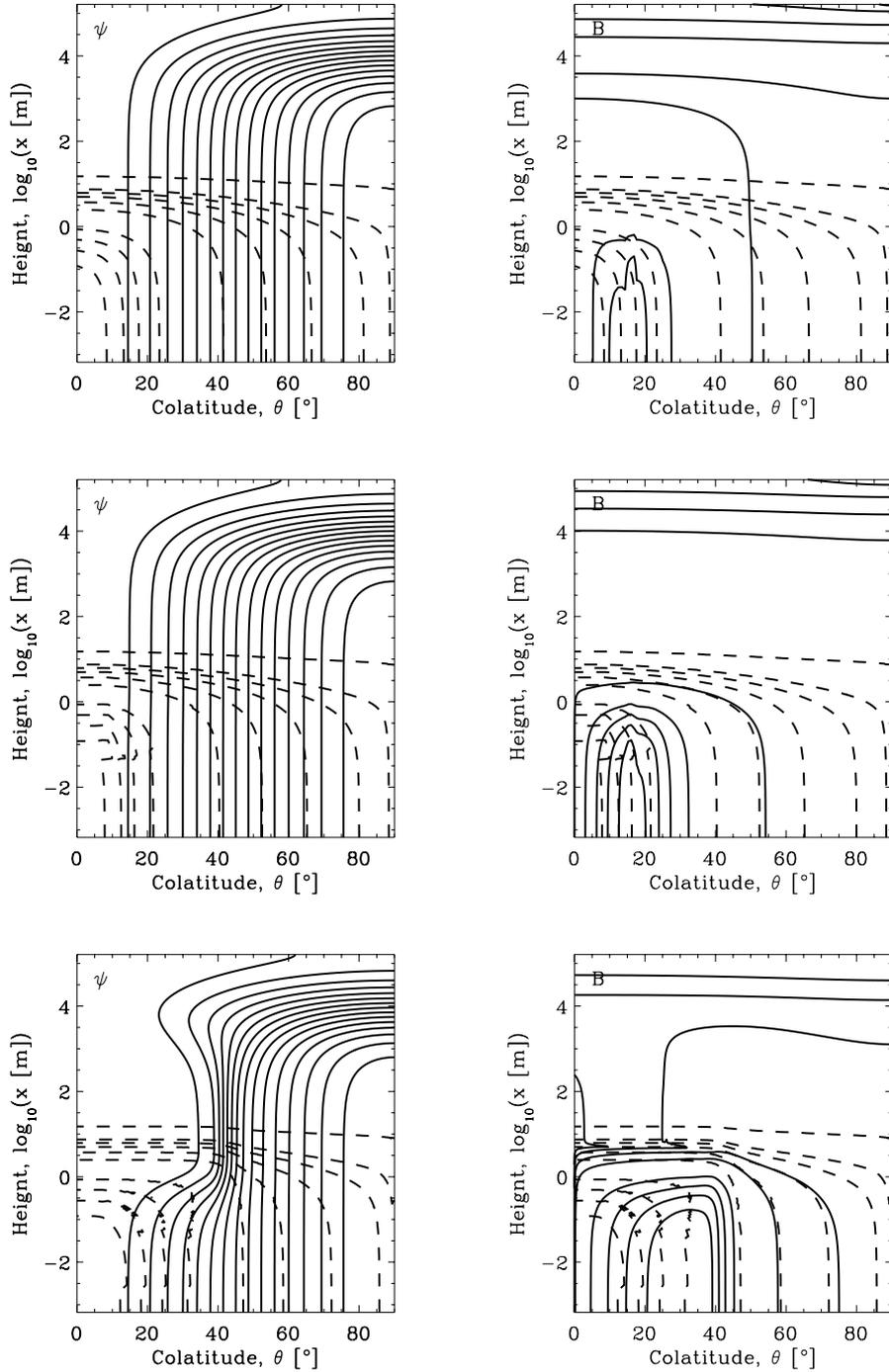
Figure 6. Magnetic configuration as a function of accreted mass. $M_a = 10^{-9}\,\mathrm{M_\odot}$, $\rho_{max} = 4.2 \times 10^{13}\,\mathrm{kg\,m^{-3}}$, $|\boldsymbol{B}|_{max} = 3.5 \times 10^8\,\mathrm{T}$ (top); $M_a = 10^{-7}\,\mathrm{M_\odot}$, $\rho_{max} = 4.2 \times 10^{15}\,\mathrm{kg\,m^{-3}}$, $|\boldsymbol{B}|_{max} = 1.1 \times 10^{10}\,\mathrm{T}$ (middle); and $M_a = 10^{-5}\,\mathrm{M_\odot}$, $\rho_{max} = 1.7 \times 10^{17}\,\mathrm{kg\,m^{-3}}$, $|\boldsymbol{B}|_{max} = 3.9 \times 10^{11}\,\mathrm{T}$ (bottom). Displayed are contours of ψ (left, solid), $|\boldsymbol{B}|$ (right, solid) and ρ (left and right, dashed). with values $\eta\rho_{max}$ and $\eta|\boldsymbol{B}|_{max}$, where $\eta = 0.8, 0.6, 0.4, 0.2, 0.01, 0.001, 10^{-4}$, $10^{-5}, 10^{-6}, 10^{-12}$.

the bubbles; on the other hand, ohmic dissipation would facilitate detachment of bubbles in a pinched, Y-point configuration.

On some runs, bubbles appear and disappear during the iteration process. This happens because the mass–flux distribution is not conserved inside a bubble, although the code attempts to maintain flux-freezing at the edge. If the route to convergence is a rough proxy for time-dependent behaviour, as argued by Mouschovias (1974) for

iterative relaxation algorithms, the appearance and disappearance of bubbles may represent evidence – though not proof – of transient evolution in reality.

As the bubbles are disconnected topologically from flux surfaces anchored to the star and accretion disc, they do not contain any accreted material (in the ideal-MHD limit of zero cross-field transport) and are lighter than their surroundings. It is therefore possible
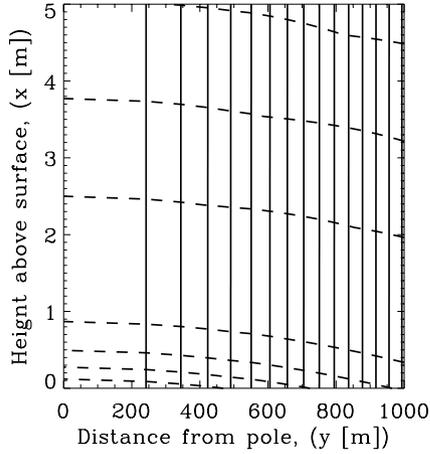
Figure 7. Magnetic field lines (solid) and density contours (dashed) around the polar cap for $M_a = 10^{-13}$ M$_\odot$ and $b = 100$; the parameters used in fig. 2 of Litwin et al. (2001).

that they rise buoyantly and ultimately escape the magnetosphere of the neutron star. This possibility cannot be investigated rigorously in the context of the equilibrium calculations in this paper; it is considered qualitatively in Section 5.3.

5 TIME-DEPENDENT EFFECTS

In this section, we discuss critically (but qualitatively) how the results of this paper may be affected by time-dependent processes that cannot be modelled by a quasi-static sequence of hydromagnetic equilibria. We consider Parker instabilities in Section 5.1, ohmic dissipation in Section 5.2, and the buoyant rise of magnetic bubbles in Section 5.3.

5.1 Hydromagnetic instabilities

The computed equilibria are manifestly distorted. Buoyancy of the compressed magnetic flux can drive long-wave, slow MHD modes that overturn the accreted matter on the Alfvén time-scale τ_A, as in the global Rayleigh–Taylor instability of the Galactic magnetic field (Parker 1966; Mouschovias 1974). When the accreted matter bends the polar magnetic field, there exists a significant component of magnetic field perpendicular to gravity, a condition for the onset of the Parker instability. In a plane-parallel geometry, wavelengths longer than $\Lambda = 4\pi x_0/(2\alpha + 1)$ are unstable (Mouschovias 1974), where $\alpha = B^2/(2\mu_0 p)$. The geometry of an accreting neutron star is far from plane-parallel. Nevertheless, in hydromagnetic equilibrium, one has $\alpha \sim 1$ locally in the boundary layer, yielding $\Lambda = 2$ m. The failure to converge at large M_a is also a hint, though not a proof, that the Parker instability may operate. Mouschovias (1974) advanced a similar convergence-based argument for the stability of a stratified vertical column with periodic boundaries.

5.2 Ohmic dissipation

Our calculations are performed under the assumption of infinite conductivity and hence flux-freezing. In reality, the accreted matter is resistive due to electron–phonon and electron–impurity scattering (Brown & Bildsten 1998; Cumming et al. 2001), potentially
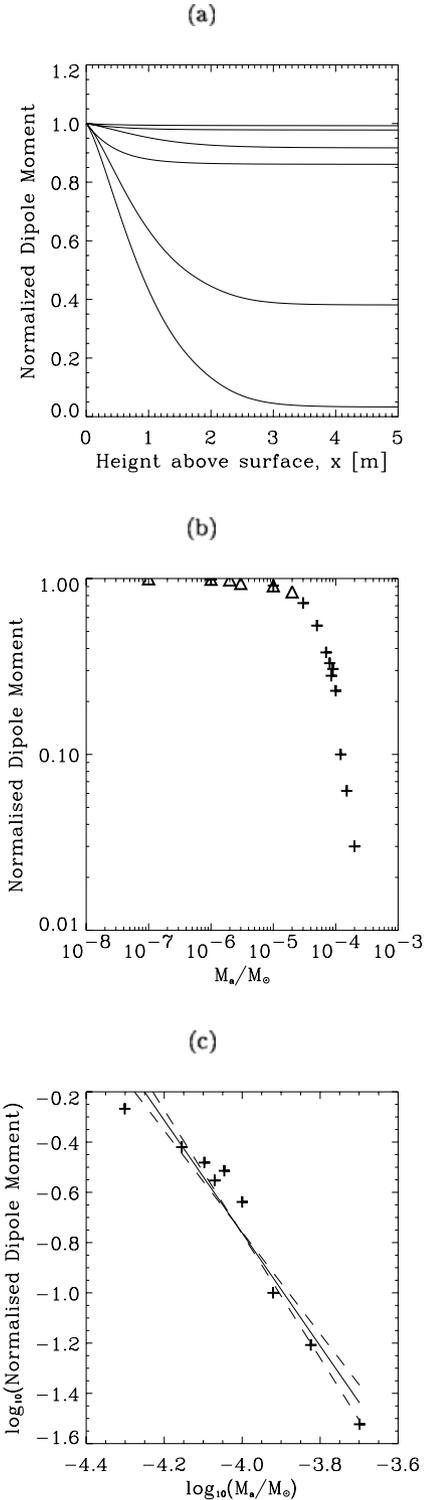
Figure 8. (a) Dipole moment $|\boldsymbol{m}|$ as a function of altitude $x = r - R_*$, normalized to $|\boldsymbol{m}|$ at $r = R_*$, for $M_a/$ M$_\odot = 10^{-6}$(top), 3×10^{-6}, 10^{-5}, 3×10^{-5}, 10^{-4}, 3×10^{-4} (bottom). (b) Dipole moment $|\boldsymbol{m}|$ as a function of accreted mass M_a, normalized to the dipole moment $|\boldsymbol{m}_i|$ before accretion, for $b = 3$ (crosses) and $b = 10$ (triangles). (c) Power-law fit (solid), with 1σ errors (dashed), to dipole moment as a function of M_a for $M_a > 2 \times 10^{-5}$ M$_\odot$.
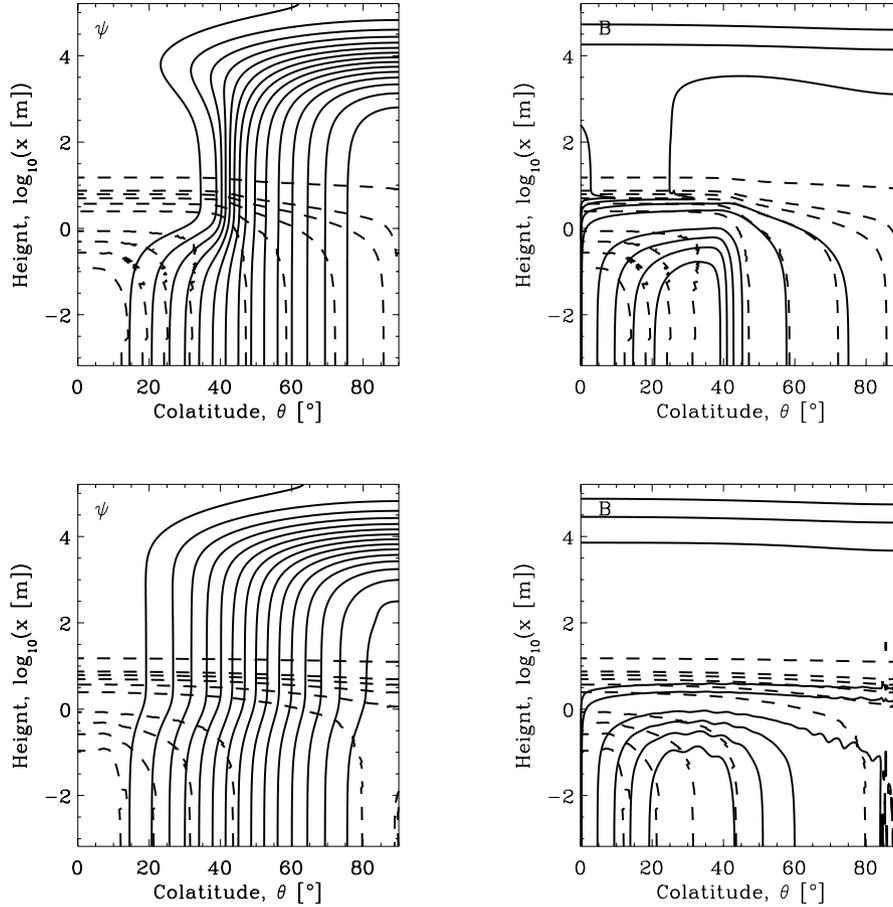
Figure 9. Hydromagnetic equilibria for $M_a = 10^{-5}$ M$_\odot$, with $b = 10$ (top) and $b = 3$ (bottom). Contours of constant ψ (left) and $|\boldsymbol{B}|$ (right) are displayed, with $|\boldsymbol{B}|_{max} = 4.06 \times 10^{11}$ T ($b = 10$) and 1.65×10^{11} T ($b = 3$). We find $|\boldsymbol{m}| \approx 0.9|\boldsymbol{m}_i|$ in both cases.
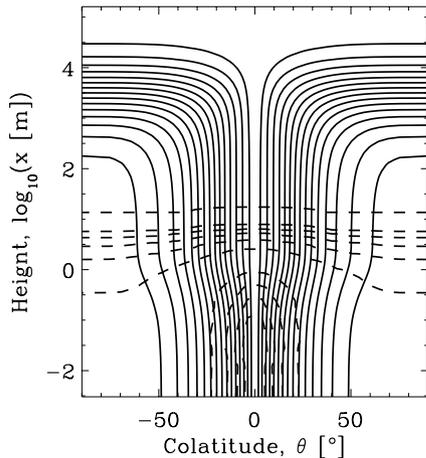
Figure 10. Equilibrium magnetic configuration in the northern hemisphere, showing contours of constant ψ (solid) and ρ (dashed). Equations (12) and (14) are solved in the domain $|\theta| \leqslant \pi/2$ here, compared to $0 \leqslant \theta \leqslant \pi/2$ in earlier figures, in order to test the validity of the $\psi = 0$ boundary condition at $\theta = 0$.

enhanced by accretion-induced heating (Romani 1990; Urpin & Geppert 1995).

The ohmic dissipation time-scale for a flux tube of width L is given by $\tau_d = \mu_0 \sigma L^2$, where σ is the electrical conductivity. For typical conditions, we take $\sigma \approx 10^{22}$ s^{-1} and hence obtain $\tau_d \approx$ $10^{14}(L/R_*)^2$s. In comparison, the flow time-scale is given by $\tau_f = 4\pi R_*^2 \rho L / \dot{M}_a$, where $\dot{M}_a$ is the accretion rate. For $\rho = 4 \times 10^{14}$ kg m^{-3}, $L = 6$ m (Section 4.4), and $\dot{M}_a = 1 \times 10^{-8}$ M$_\odot$yr^{-1}, we find $\tau_f = 1 \times 10^2$ yr. Therefore, for the length-scales characteristic of the compressed flux layer, we have $\tau_f > \tau_d$ and magnetic flux diffuses through the accreted material, broadening the compressed flux layer until it is thick enough ($L \approx 600$ m) that $\tau_d \approx \tau_f$ and further thickening ceases. Brown & Bildsten (1998) showed that τ_f/τ_d depends only on $\dot{M}_a$ and not on depth in the crust.

Note that the buried flux is resurrected on the time-scale τ_d, after accretion stops. As the noted dipole field reasserts itself, $|\boldsymbol{m}|$ increases. A full analysis of this process is left to future work.

5.3 Buoyant bubbles

Closed magnetic bubbles have $\rho = 0$ within and are lighter than their surroundings, as discussed in Section 4.7. They tend to rise buoyantly at the local Alfvén speed $v_A = (B^2/\mu_0\rho)^{1/2} = c_s(2\alpha)^{1/2}$, and hence escape the magnetosphere in ≈ 2 yr. Assuming an accretion rate of 10^{-8} M$_\odot$ yr^{-1}, it takes $\approx 10^4 b^{-1}(\dot{M}_a/10^{-8}M_\odot$yr$^{-1})^{-1}$ yr to accrete enough mass to create one bubble. Moreover, a typical bubble encloses $\approx\psi_a$ of magnetic flux. Hence we conclude that magnetic flux is being expelled episodically from the magnetosphere at an average rate of $10^{11}(\psi_*/10^{16}$ Tm$^2)(\dot{M}_a/10^{-8}$ M$_\odot$ yr$^{-1})^{-1}$ T m^2 yr^{-1}. Note that expelled flux is subsequently replenished by the current deep in the star (since ψ is fixed at the surface).
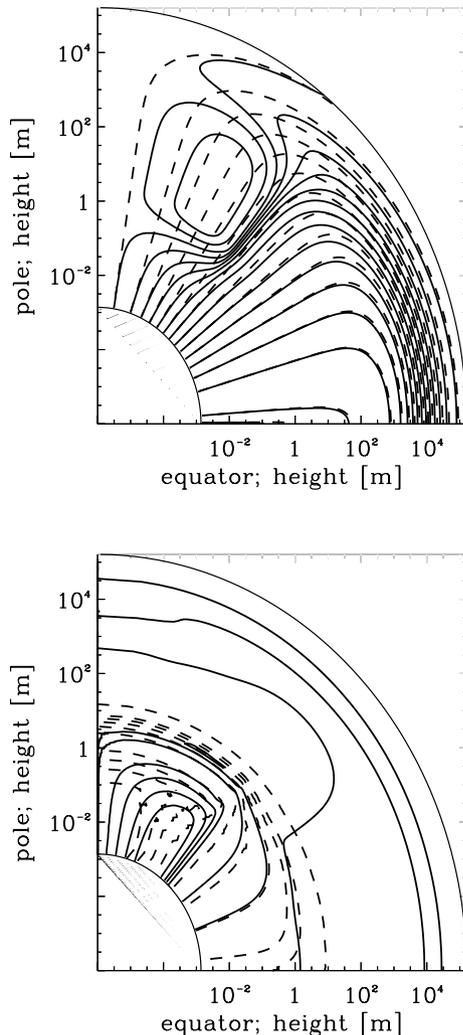
Figure 11. Magnetic configuration for $M_a = 2 \times 10^{-5}$ M$_\odot$, $b = 10$, showing the creation of a bubble. We plot contours of constant ψ (top) for initial (dashed) and final (solid) states, and final $|\boldsymbol{B}|$ contours $\eta\,|\boldsymbol{B}|_{max}$ (bottom, solid) and ρ contours (dashed) $\eta\rho_{max}$; $\rho_{max} = 5 \times 10^{17}$ kg m^{-3}, $B_{max} = 6.3 \times 10^{11}$ T, and $\eta = 0.8, 0.6, 0.4, 0.2, 0.01, 0.001, 10^{-4}, 10^{-5}, 10^{-6}, 10^{-12}$.

6 CONCLUSION

Observations of low-field binary neutron stars and recycled pulsars imply that the magnetic dipole moment of a neutron star is reduced by accretion. In this paper, we undertake a self-consistent analysis (numerical and analytic) of one mechanism that may account for the reduction observed: polar magnetic burial in the ideal-magnetohydrodynamic regime. Our analysis has several new features.

(i) Flux-freezing is strictly enforced when connecting the final and initial magnetic configurations by solving self-consistently for the mass–flux distribution rather than specifying it ad hoc (see Fig. 5).

(ii) The Lorentz force due to equatorial magnetic field lines compressed by equatorward hydromagnetic spreading is included when calculating the confinement of the polar accreted column.

(iii) Numerical methods are developed for treating accreted masses up to $\approx 10^{-4}$ M$_\odot$ (cf. 10^{-10} M$_\odot$ in previous work), where the field is dramatically distorted and high-order multipoles dominate.

We report two key results.

(i) $M_a \gtrsim 10^{-5}$ M$_\odot$ must be accreted in order to reduce significantly the magnetic dipole moment $|\boldsymbol{m}|$ of the star, contrary to previous estimates ($M_a \approx 10^{-10}$ M$_\odot$) which neglected equatorial magnetic stresses. For small M_a, we find $|\boldsymbol{m}| = |\boldsymbol{m}_i|(1 - M_a/M_c)$, with $M_c = 1.2 \times 10^{-6}$ M$_\odot$, (cf. Shibazaki et al. 1989). For $M_c \lesssim M_a \lesssim 10^{-4}$ M$_\odot$, we find $|\boldsymbol{m}| = |\boldsymbol{m}_i|(M_a/4.6 \times 10^{-5}$ M$_\odot)^{2.25\pm0.22}$.

(ii) When enough mass is accreted, such that $M_a \gtrsim 10^{-4}b^{-1}$ M$_\odot$, the hydrostatic pressure gradient generates flux surfaces with $\psi < 0$ or $\psi > \psi_*$, creating closed magnetic bubbles that are disconnected topologically from the stellar surface. The bubbles are valid solutions of the Grad–Shafranov boundary problem, as confirmed by analytic, Green function calculations; they are not numerical artefacts or fingerprints of hydromagnetic instabilities (e.g. Parker).

Several of our assumptions need to be relaxed in future work, including

(i) perfect conductivity,

(ii) an impenetrable stellar surface, and

(iii) axisymmetry (which tends to suppress hydromagnetic instabilities, for example).

Finally, the uniqueness of the hydromagnetic equilibria we compute numerically is yet to be established.

Our equilibria serve as useful starting points for exploring the stability of the magnetic configuration during and after accretion. Our theoretical results will be tested against observational data from binary neutron stars and recycled pulsars in a companion paper.

REFERENCES

Arons J., Burnard D. J., Klein R. I., McKee C. F., Pudritz R. E., Lea S. M., 1984, in Woosley S. E., ed., High Energy Transients in Astrophysics. Am. Inst. Phys., New York, p. 215
Arons J., Lea S. M., 1980, ApJ, 235, 1016
Basko M. M., Sunyaev R. A., 1976, SvA, 20, 537
Bernstein I. B., Frieman E., Kruskal M., 1958, Proc. R. Soc. London A, 244, 17
Bhattacharya D., 1999, in Arzoumanian Z., Van der Hooft F., van den Heuvel E. P. J., eds, Pulsar Timing, General Relativity and the Internal Structure of Neutron Stars. Koninklijke Netherlands Akademie van Wetenschappen, the Netherlands, p. 235
Blondin J. M., Freese K., 1986, Nat, 323, 786
Brown E. F., Bildsten L., 1998, ApJ, 496, 915
Cheng K. S., Zhang C. M., 1998, A&A, 337, 441
Choudhuri A. R., Konar S., 2002, MNRAS, 332, 933
Cumming A., 2002, MNRAS, 333, 589
Cumming A., Zweibel E., Bildsten L., 2001, ApJ, 557, 958
Dungey J., 1953, MNRAS, 113, 180
Geppert U., Rheinhardt M., 2002, A&A, 392, 1015
Ghosh P., Lamb F. K., 1979, ApJ, 234, 296
Hameury J. M., Bonazzola S., Heyvaerts J., Lasota J. P., 1983, A&A, 128, 369
Hartman J. W., Bhattacharya D., Wijers R., Verbunt F., 1997, A&A, 322, 477
Klimchuk J. A., Sturrock P. A., 1989, ApJ, 345, 1034
Konenkov D., Geppert U., 2001, MNRAS, 325, 426
Litwin C., Brown E. F., Rosner R., 2001, ApJ, 553, 788
Low B. C., 1980, Sol. Phys., 65, 147

Melatos A., Phinney E. S., 2001, Publ. Astron. Soc. Aust., 18, 421

Morse P. M., Feshbach H., 1953, Methods of Theoretical Physics. McGraw-Hill, New York

Mouschovias T., 1974, ApJ, 192, 37

Muslimov A. G., Tsygan A. I., 1985, SvAL, 11, 80

Parker E., 1966, ApJ, 145, 811

Press W. H., Teukolsky S. A., Vetterling W. T., Flannery B. P., 1992, Numerical Recipes in C. The Art of Scientific Computing. Cambridge Univ. Press, Cambridge

Rastätter L., Schindler K., 1999, ApJ, 519, 658

Romani R. W., 1990, Nat, 347, 741

Shibazaki N., Murakami T., Shaham J., Nomoto K., 1989, Nat, 342, 656

Snyder W. V., 1978, ACM Trans. Math. Soft., 4, 290

Srinivasan G., Bhattacharya D., Muslimov A., Tsygan A., 1990, Curr. Sci., 59, 31

Taam R. E., van den Heuvel E. P. J., 1986, ApJ, 305, 235

Thompson C., Duncan R. C., 1993, ApJ, 408, 194

Uchida Y., Low B. C., 1981, JA&A, 2, 405

Urpin V., Geppert U., 1995, MNRAS, 275, 1117

Urpin V., Konenkov D., 1997, MNRAS, 284, 741

van den Heuvel E. P. J., Bitzaraki O., 1995, A&A, 297, L41

Wijers R. A. M. J., 1997, MNRAS, 287, 607

Zweibel E. G., Hundhausen A. J., 1982, Sol. Phys., 76, 261

APPENDIX A: ANALYTIC SOLUTION OF THE GRAD–SHAFRANOV PROBLEM

In this appendix, we solve the Grad–Shafranov equation (12), together with the boundary conditions (17), by a Green function approach.

A1 Green theorem for the Grad–Shafranov operator

An operator $L\psi = \nabla^2\psi + \boldsymbol{b}\cdot\nabla\psi + c\psi$, acting on a function ψ, possesses an adjoint $L^*\psi = \nabla^2\psi - \nabla\cdot(\boldsymbol{b}\psi) + c\psi$. The Grad–Shafranov operator $L = \mu_0 r^2 \sin^2\theta\,\Delta^2$, defined by (17) in spherical polar coordinates, has $\boldsymbol{b} = -2r^{-1}(\hat{\boldsymbol{e}}_r + \cot\theta\hat{\boldsymbol{e}}_\theta)$ and is not self-adjoint (cf. ∇^2). Letting G and G^* be the Green functions associated with the operators L and L^*, respectively,

$$LG(\boldsymbol{x},\boldsymbol{x}') = \delta(\boldsymbol{x}-\boldsymbol{x}'), \tag{A1}$$

$$L^*G^*(\boldsymbol{x},\boldsymbol{x}') = \delta(\boldsymbol{x}-\boldsymbol{x}'), \tag{A2}$$

related by the reciprocity relation $G^*(\boldsymbol{x},\boldsymbol{x}') = G(\boldsymbol{x}',\boldsymbol{x})$, we arrive at the Lagrange identity

$$\psi L^*G^* - G^*L\psi = \nabla\cdot(\psi\nabla G^* - G^*\nabla\psi + \boldsymbol{b}\psi G^*). \tag{A3}$$

Upon integrating (A3) over a volume V, bounded by a surface S, and using the divergence theorem, we obtain

$$\int_V (\psi L^*G^* - G^*L\psi)\,\mathrm{d}V$$
$$= \int_S (\psi\nabla G^* - G^*\nabla\psi + \boldsymbol{b}\psi G^*)\cdot\hat{\boldsymbol{n}}\,\mathrm{d}S, \tag{A4}$$

where $\hat{\boldsymbol{n}}$ is the unit vector normal to S. Given a boundary value problem $L\psi(\boldsymbol{x}) = Q(\boldsymbol{x})$ in the volume V, with ψ given on the boundary S, we combine (A2) and (A4) to obtain

$$\psi(\boldsymbol{x}) = \int_V \mathrm{d}^3\boldsymbol{x}'\,G^*Q$$
$$+ \int_S \mathrm{d}^2\boldsymbol{x}'\hat{\boldsymbol{n}}\cdot(\psi\nabla G^* - G^*\nabla\psi + \boldsymbol{b}\psi G^*). \tag{A5}$$

A2 Green function for the Grad–Shafranov equation

We wish to solve (12) for ψ in $r \geqslant R_*$ subject to Dirichlet boundary conditions (17) on ψ at $r = R_*$ and $r \to \infty$. In cylindrical symmetry, the volume and surface integrals in (20) reduce to surface and line integrals, respectively. It is convenient to make the substitution $\mu = \cos\theta$, whereupon (12) becomes

$$\frac{\partial^2\psi}{\partial r^2} + \frac{(1-\mu^2)}{r^2}\frac{\partial^2\psi}{\partial\mu^2} = \mu_0 r^2(1-\mu^2)\frac{\mathrm{d}F(\psi)}{\mathrm{d}\psi}$$
$$\times \exp\left(-\phi_0/c_s^2 - GMr/R_*^2 c_s^2\right) \tag{A6}$$

and $\mathrm{d}F/\mathrm{d}\psi$ is a function of r and μ through $\psi(r,\mu)$.

We redefine L to be the operator on the left-hand side of (A6), and $Q(r,\mu)$ to be the source term on the right-hand side, known explicitly once $F(\psi)$ is known. The Green function G for L satisfies

$$\frac{\partial^2 G}{\partial r^2} + \frac{(1-\mu^2)}{r^2}\frac{\partial^2 G}{\partial\mu^2} = \frac{1}{r^2}\delta(r-r')\delta(\mu-\mu') \tag{A7}$$

and the Green function G^* for L^* satisfies

$$\frac{\partial^2 G^*}{\partial r^2} + \frac{(1-\mu^2)}{r^2}\frac{\partial^2 G^*}{\partial\mu^2} + \frac{4}{r}\frac{\partial G^*}{\partial r} - \frac{4\mu}{r^2}\frac{\partial G^*}{\partial\mu}$$
$$= \frac{1}{r^2}\delta(r-r')\delta(\mu-\mu'). \tag{A8}$$

Equation (A8) is separable. We expand the solution in terms of orthogonal Gegenbauer polynomials $C_\ell^{3/2}(\mu)$, viz.

$$G(r,\mu,r',\mu') = \sum_{\ell=0}^{\infty} g_\ell(r,r') \times (1-\mu^2)C_\ell^{3/2}(\mu')C_\ell^{3/2}(\mu), \tag{A9}$$

with

$$\frac{\mathrm{d}^2 g_\ell(r,r')}{\mathrm{d}r^2} - \frac{\ell(\ell+1)}{r^2}g_\ell(r,r') = r^{-2}\delta(r-r'). \tag{A10}$$

The Gegenbauer polynomials satisfy

$$(1-\mu^2)\frac{\mathrm{d}^2}{\mathrm{d}\mu^2}\left[(1-\mu^2)C_{\ell-1}^{3/2}(\mu)\right] + \ell(\ell+1)[(1-\mu^2)C_{\ell-1}^{3/2}(\mu)] = 0 \tag{A11}$$

and are related to associated Legendre polynomials via $P_\ell^1(\mu) = -(1-\mu^2)^{1/2}C_{\ell-1}^{3/2}(\mu)$. The first few are listed for reference: $C_0^{3/2}(\mu) = 1$, $C_1^{3/2}(\mu) = 3\mu$, $C_2^{3/2}(\mu) = 3/2(5\mu^2-1)$, $C_3^{3/2}(\mu) = 5/2(7\mu^3 - 3\mu)$, $C_4^{3/2}(\mu) = 15/4(21\mu^4 - 14\mu^2 + 1)$, $C_5^{3/2}(\mu) = 3/8(231\mu^5 - 210\mu^3 + 35\mu)$. They satisfy an orthogonality condition:

$$\int_{-1}^{1}(1-\mu^2)C_\ell^{3/2}(\mu)C_{\ell'}^{3/2}(\mu)\,\mathrm{d}\mu = N_\ell\delta_{\ell\ell'} \tag{A12}$$

with

$$N_\ell = \frac{2(\ell+1)(\ell+2)}{(2\ell+3)}. \tag{A13}$$

We solve (A10) for $g_\ell(r,r')$ subject to the following conditions:

(i) $g_\ell(r,r')$ is continuous at $r = r'$,
(ii) $\lim_{\epsilon\to 0}[\mathrm{d}g_\ell(r,r')/\mathrm{d}r]_{r'-\epsilon}^{r'+\epsilon} = r'^{-2}$, and
(iii) $g_\ell(R_*,r') = 0$, and (iv) $\lim_{r\to\infty}g_\ell(r,r') = 0$.

The result is

$$g_\ell(r,r') = \frac{1}{(2\ell+1)r'^2}\frac{r_<^{\ell+1}}{r_>^\ell}\left[\left(\frac{R_*}{r_<}\right)^{2\ell+1} - 1\right], \tag{A14}$$

with $r_< = \min(r, r')$ and $r_> = \max(r, r')$, yielding

$$G(r, \mu, r', \mu') = \sum_{\ell=0}^{\infty} N_\ell^{-1} g_{\ell+1}(r, r') \times (1 - \mu'^2) C_\ell^{3/2}(\mu') C_\ell^{3/2}(\mu). \tag{A15}$$

Similarly, we obtain

$$G^*(r, \mu, r', \mu') = \sum_{\ell=0}^{\infty} N_\ell^{-1} g_\ell^*(r, r') \times (1 - \mu'^2) C_\ell^{3/2}(\mu') C_\ell^{3/2}(\mu), \tag{A16}$$

with $G^*{}_\ell(r, r') = (r'/r)^2 g_{\ell+1}(r, r')$. Equations (A15) and (A16) are consistent with the reciprocity relation. Note that basis functions for G and G^* for a non-self-adjoint operator are mutually but not individually orthogonal (Morse & Feshbach 1953).

Upon combining the Green theorem (A4), the definition of G^* (A16), the boundary conditions $\psi(R_*, \mu) = \psi_*(1 - \mu^2)$, $\psi(r, \pm 1) = 0$, $\lim_{r\to\infty} \psi(r, \mu) = 0$, $G^*(R_*, \mu, r', \mu') = 0$, and the surface gradient $\nabla\psi(r, \pm 1) \cdot \hat{e}_\mu = 0$, we find that the boundary integral over C reduces to $\int_{-1}^{1} \psi(R_*, \mu)(\partial G^*/\partial r)\, d\mu'$, yielding the complete solution

$$\psi(r, \mu) = \psi_* R_* \frac{(1 - \mu^2)}{r} + (1 - \mu^2) \sum_{\ell=0}^{\infty} N_\ell^{-1} C_\ell^{3/2}(\mu)$$
$$\times \int_{-1}^{1} d\mu' \int_{R_*}^{\infty} dr' r'^2 g_\ell^*(r', r) C_\ell^{3/2}(\mu') Q(r', \mu'). \tag{A17}$$

A3 Small-M_a limit: constant source term

To explore the form of the general solution (28), in the small-M_a limit, we linearize $F(\psi)$. We consider the special case $F(\psi) = Q_0(\psi_* - \psi)$, giving $Q(r, \mu) = Q_0(1 - \mu^2)r^2 e^{-r}$. By orthogonality, only the $\ell = 0$ term survives. We find

$$\int_{R_*}^{\infty} g_1(r, r') r'^4 e^{-r'} dr' = -\frac{1}{r}[f_1(r) - f_1(R_*)], \tag{A18}$$

with $f_1(r) = (r^3 + 4r^2 + 8r + 8)\,e^{-r}$, and hence

$$\psi(r, \mu) = \psi_* R_* \frac{(1 - \mu^2)}{r}\left\{1 - \frac{Q_0}{4\psi_* R_*}[f_1(r) - f_1(R_*)]\right\}, \tag{A19}$$

using $N_1 = 4/3$. It is immediately clear that negative values of ψ are possible if $Q_0 > 4\psi_* R_*[f_1(r) - f_1(R_*)]$ raising the possibility of closed magnetic loops (bubbles) constructed from flux surfaces $\psi < 0$ or $\psi > \psi_*$ and hence not anchored to the stellar surface.

In dimensionless coordinates, setting $\tilde{F}(\tilde{\psi}) = k(b - \tilde{\psi})$ we arrive at

$$\tilde{\psi}(\tilde{x}, \tilde{\mu}) = \tilde{\psi}_i(\tilde{x}, \tilde{\mu})\left\{1 + \frac{kQ_0 a^2}{b}\left[f_1(\tilde{x})e^{-\tilde{x}} - f_2(a)(1 - e^{-\tilde{x}})\right]\right\}, \tag{A20}$$

where $f_1(\tilde{x}) = 3\tilde{x}a^{-1} + a^{-2}(3\tilde{x}^2 + 8\tilde{x}) + a^{-3}(\tilde{x}^3 + 4\tilde{x}^2 + 8\tilde{x})$ and $f_2(a) = 1 + 4a^{-1} + 8a^{-2} + 8a^{-3}$. For $\tilde{x} \ll a$, where the screening currents dominate, $\tilde{\psi}$ reduces to $\tilde{\psi}_i(\tilde{x}, \tilde{\mu})[1 - kQ_0 a^2 b^{-1}(1 - e^{-\tilde{x}})]$. In Appendix A4, we show that $k \approx b/(2\pi a^2)$, so the reduction factor is $(1 - b^2 M_a/M_c)$, remembering that $Q_0 \propto M_a$. For neutron-star parameters, one has $M_c \approx 1.2 \times 10^{-4}\, M_\odot$.

We can estimate the thickness of the compressed flux layer, x_b, in the small-M_a regime by solving $\tilde{\psi}(x_b, \tilde{\mu}) = 0$ to give $x_b = -\ln(1 -$

$M_c/M_a)$. We may also estimate when $|\mathbf{B}|$ changes significantly from its initial value $|\mathbf{B}_i|$. Near the surface, the principal component

$$B_\mu = (B_i)_\mu[ab^2 M_a/M_c e^{-\tilde{x}} + 1 - b^2 M_a/M_c(1 - e^{-\tilde{x}})] \tag{A21}$$

increases significantly for $M_c/a \gtrsim 8 \times 10^{-11}\, M_\odot$, consistent with the numerical results in Section 3. Setting $B_\mu = 0$ gives an alternative estimate of the altitude below which the screening currents are confined, with $\tilde{x} = \ln[(a + 1)/(1 - b^2 M_c/M_a)] = 9.8$ consistent with (A21). Including also the radial component B_r, we obtain

$$B = B_i\left[4\mu^2\left(1 - b^2 M_a/M_c(1 - e^{-\tilde{x}})\right)^2 + (1 - \mu^2)\left(1 + ab^2 M_a/M_c e^{-\tilde{x}}\right)^2\right]^{1/2}, \tag{A22}$$

which reduces to

$$B = B_i\left[4\mu^2 + (1 - \mu^2)\left(ab^2 M_a/M_c\right)^2\right]^{1/2} \tag{A23}$$

near the surface for $10^{-10} \leqslant M_a/M_c \leqslant 10^{-6}$. There is also a boundary layer at the magnetic pole, where B_μ increases rapidly from zero over a short distance. The width of this polar boundary layer may be estimated by setting $B_\mu \approx B_r$, yielding $\approx \pi R_* \tan^{-1}[2M_c/(ab^2\, M_a)] \approx 20$ m.

A4 Dipole field

A useful analytic approximation to the source term $dF/d\psi$ can be derived for the dipole field in the early stages of accretion. In dimensionless coordinates, defined in Appendix B, (16) becomes

$$\tilde{\psi}_i(\tilde{x}, \tilde{\mu}) = b(1 - \tilde{\mu}^2)(1 + \tilde{x}/a)^{-1} \tag{A24}$$

with $a = R_*/x_0$ and $b = \psi_*/\psi_a$. From (14), we write $d\tilde{M}/d\tilde{\psi} = \tilde{F}(\tilde{\psi})I(\tilde{\psi})$, with

$$I(\tilde{\psi}) = 2\pi \int_C d\tilde{s}(1 - \tilde{\mu}^2)^{1/2}(\tilde{x} + a)e^{-\tilde{x}}|\tilde{\nabla}\tilde{\psi}|^{-1}. \tag{A25}$$

C is a contour of constant ψ, along which we may write $\tilde{\mu} = [1 - \tilde{\psi}\tilde{r}/(ab)]^{1/2}$; the integral terminates at $\tilde{x} = 0$ on the surface and $\tilde{x} = a(b/\tilde{\psi} - 1)$ above the equator. Upon rearranging we obtain

$$I(\tilde{\psi}) = \pi a^2 J(\tilde{\psi}) b^{-1/2}(b - \tilde{\psi})^{-1/2} \tag{A26}$$

with

$$J(\tilde{\psi}) = \int_0^{a(b/\tilde{\psi}-1)} d\tilde{x}(1 + \tilde{x}/a)^3 e^{-\tilde{x}}\left[1 - \frac{\tilde{x}\tilde{\psi}}{a(b - \tilde{\psi})}\right]^{-1/2} \tag{A27}$$

The function $J(\tilde{\psi})$ is plotted in Fig. A1. We observe that $J \approx 1$ for all $\tilde{\psi}$ except near the equator. Its limiting behaviour is $I(\tilde{\psi}) \to \pi a^2 b^{-1}$ as $\tilde{\psi} \to 0$, and $I(\tilde{\psi}) \to 2\pi a^3(b - \tilde{\psi})^{1/2}b^{-3/2}$ as $\tilde{\psi} \to b$. If we choose $d\tilde{M}/d\tilde{\psi} = \exp(-\tilde{\psi})/2$ specifically, then from (A25) we have

$$\tilde{F}(\tilde{\psi}) = \frac{b}{2\pi a^2}\exp(-\tilde{\psi})(1 - \tilde{\psi}/b)^{1/2}[J(\tilde{\psi})]^{-1}. \tag{A28}$$

Upon differentiating with respect to $\tilde{\psi}$, we obtain

$$\frac{d\tilde{F}}{d\tilde{\psi}} = -\frac{be^{-\tilde{\psi}}}{2\pi a^2}\left\{(1 - \tilde{\psi}/b)^{-1/2}\,[1 + (1 - 2\tilde{\psi})/(2b)][J(\tilde{\psi})]^{-1}\right.$$
$$\left. - (1 - \tilde{\psi}/b)^{1/2}[J(\tilde{\psi})]^{-2}J'(\tilde{\psi})\right\}. \tag{A29}$$
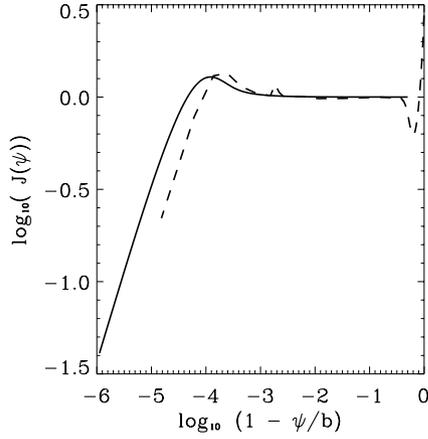
Figure A1. The function $J(\tilde{\psi})$ (solid) compared with $J(\tilde{\psi})$ calculated numerically for $M_a = 10^{-5}$ M$_\odot$, $b = 10$ (dashed).

APPENDIX B: ITERATIVE NUMERICAL SCHEME

B1 Dimensionless equations and logarithmic coordinates

It is convenient to convert to dimensionless variables $\tilde{x} = (r - R_*)/x_0$, $\tilde{\psi} = \psi/\psi_a$, $\tilde{M} = M/M_a$, $\tilde{\mu} = \cos\theta$, $\tilde{F} = F/F_0$ and $\tilde{\boldsymbol{B}} = \boldsymbol{B}/B_0$ where $x_0 = c_s^2 R_*^2/(GM_*)$ is the pressure scaleheight, $a = R_*/x_0$, $F_0 = M_a c_s^2/x_0^3$, and $B_0 = \psi_a/r_0^2 = a^2 B_*/2b$. Equations (12) and (14) take the forms

$$\frac{\partial^2 \tilde{\psi}}{\partial \tilde{x}^2} + \frac{(1 - \tilde{\mu}^2)}{(\tilde{x} + a)^2}\frac{\partial^2 \tilde{\psi}}{\partial \tilde{\mu}^2} = -Q_0(1 - \tilde{\mu}^2)(\tilde{x} + a)^2 e^{-\tilde{x}}\frac{\mathrm{d}\tilde{F}}{\mathrm{d}\tilde{\psi}} \qquad \text{(B1)}$$

and

$$\frac{\mathrm{d}\tilde{M}}{\mathrm{d}\tilde{\psi}} = 2\pi\tilde{F}(\tilde{\psi})\int_C \mathrm{d}\tilde{s}(1 - \tilde{\mu}^2)^{1/2}(\tilde{x} + a)e^{-\tilde{x}}|\tilde{\nabla}\tilde{\psi}|^{-1}, \qquad \text{(B2)}$$

respectively, with $Q_0 = \mu_0 x_0 M_a c_s^2/\psi_a^2$. Note that μ_0 denotes the permeability of free space (SI units).

As M_a increases, a thin boundary layer of screening currents forms near the surface of the neutron star (see Section 4, and Melatos & Phinney 2001). To concentrate maximum grid resolution at the boundary layer and at the edge of the polar cap ($\psi = \psi_a$), where the gradients of ρ and ψ are steepest, we scale the r and θ coordinates logarithmically, such that

$$\tilde{x}_1 = \log(\tilde{x} + e^{-L_x}) + L_x, \qquad \text{(B3)}$$

$$\tilde{y}_1 = -\log[1 - (1 - e^{-L_y})\tilde{y}]. \qquad \text{(B4)}$$

L_x must be chosen sufficiently small to ensure at least several nodes per hydrostatic (or hydromagnetic) scaleheight. To resolve steep gradients at the equator, a similar transformation exists.

B2 Grid and Poisson equation

We use a grid of (G_x, G_y) cells in (r, θ) and N_c contours of ψ, and choose $N_c \leqslant G_x$ to avoid zig-zags in $I(\psi)$ due to grid crossings which damage convergence (Fig. B1). We typically set $G_x = G_y = 256$ and $N_c = 255$, with the contour values chosen to lie between grid-points at the stellar surface.

Given M_a and hence $\mathrm{d}M/\mathrm{d}\psi$, and starting with a guess $\psi^{(0)}(r, \theta)$, the left-hand side of (12), $\Delta^2\psi^{(0)}$, can be calculated at each grid-point. The resulting Poisson equation is solved using a successive overrelaxation procedure with Chebychev acceleration (Press
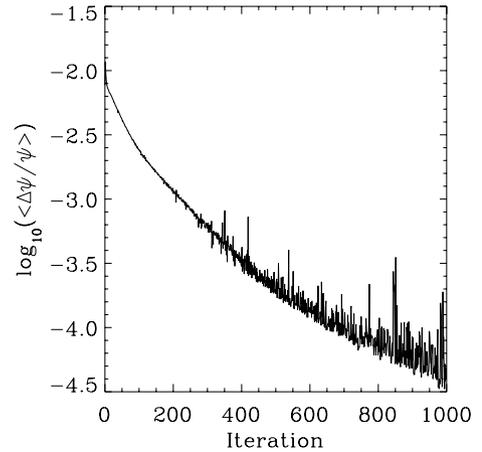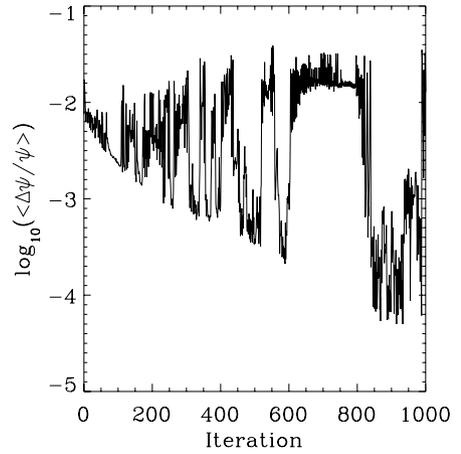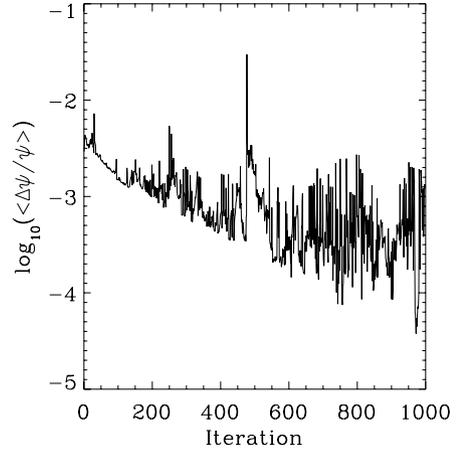
Figure B1. Comparison of convergence for $\Theta = 0.995$, $b = 3$, $M_a = 8.5 \times 10^{-5}$ M$_\odot$. (i) $G = 64$, $N_c = 63$ (top). (ii) $G = 64$, $N_c = 255$ (middle). (iii) $G = 256$, $N_c = 255$ (bottom).

et al. 1992), stopping when the mean residual over the grid satisfies $\langle\Delta\psi/\psi\rangle \leqslant \epsilon = 10^{-2}$.

B3 Grad–Shafranov source term and contouring

To find the source term on the right-hand side of (12), $F(\psi)$ is calculated from (14). The integral along ψ contours relies on a

Table B1. Optimal $\Theta^{(n)}$ values as a function of M_a and b.

b	$M_a/\mathrm{M}_\odot$			
	10^{-10}	10^{-6}	10^{-5}	10^{-4}
3	0.0	0.5	0.9	0.995
10	0.0	0.8	0.99	0.99999
30	0.0	0.99	0.999	—

Table B2. Average and maximum errors as a function of grid size.

Grid size	Mean $(\Delta\psi/\psi)$	Max $(\Delta\psi/\psi)$
8	0.060 3082	0.229 865
16	0.016 6787	0.121 939
32	0.003 079 97	0.022 2018
64	0.001 299 22	0.032 8857
128	0.000 404 714	0.005 897 75
256	0.000 286 883	0.010 4630

contouring algorithm adapted from Snyder (1978), which can follow closed loops and topologically disconnected contours. Numerical differentiation of $F(\psi)$ by first- or second-order differencing leads to numerical problems, magnifying small fluctuations in $I(\psi)$ and hence $F(\psi)$. We overcome this by smoothing $F(\psi)$ at each iteration step, fitting an order N_p polynomial ($N_p = 10$ typically) to $[I(\psi)]^{-1}$, viz. $[I(\psi)]^{-1} = \sum_{i=0}^{N_p} a_i (\log \psi)^i$, and then differentiating $F(\psi) = [I(\psi)]^{-1} \, \mathrm{d}M/\mathrm{d}\psi$ analytically.

B4 Underrelaxation

The contour values of $\mathrm{d}F/\mathrm{d}\psi$ are mapped on to the grid by linear interpolation and fed into (12) by underrelaxation, viz.

$$\Delta^2 \psi_{\mathrm{new}}^{(n+1)} = -F'[\psi^{(n)}] \exp\left[-(\phi - \phi_0)/c_s^2\right], \tag{B5}$$

$$\psi^{(n+1)} = \Theta^{(n)} \psi^{(n)} + [1 - \Theta^{(n)}] \psi_{\mathrm{new}}^{(n)}, \tag{B6}$$

where $\psi_{\mathrm{new}}^{(n)}$ is a provisional iterate and $0 \leqslant \Theta^{(n)} \leqslant 1$ is the underrelaxation parameter at the nth iteration. Convergence is reached when

$$\left|\psi_{\mathrm{new}}^{(n+1)} - \psi^{(n)}\right| < \epsilon \left|\psi_{\mathrm{new}}^{(n+1)}\right| \tag{B7}$$

is satisfied for all grid-points. As a rule of thumb, we take $\epsilon = 10^{-2}(M_a/10^{-6}\,\mathrm{M}_\odot)$; our solutions do not converge reliably for $M_a \gtrsim 10^{-4}\,\mathrm{M}_\odot$. The stability of the solution is checked by perturbing it slightly and looking for reconvergence, or by resetting $\Theta^{(n)} \approx 0$.

The optimal value of $\Theta^{(n)}$ is governed by maximum ψ gradient between grid-points, which in turn depends on M_a. We adjust $\Theta^{(n)}$ towards unity when $|\psi_{\mathrm{new}}^{(n+1)} - \psi^{(n)}|$ tends to increase. Table B1 shows approximate optimal values of Θ for different input parameters, chosen to minimize the number of iterations while still achieving convergence.

B5 Testing and convergence

We tested the code by successfully reproducing the final equilibrium states of the Parker instability, plotted in fig. 2 of Mouschovias (1974), to an accuracy of 1 per cent. We also tested the code against the exact analytic solution (A19) in Appendix A for constant $\mathrm{d}F/\mathrm{d}\psi$. Table B2 shows a comparison of the mean and maximum errors as a function of grid size, relative to (A19), when solving the Poisson equation directly [$\Theta^{(n)} = 0$].

This paper has been typeset from a TEX/LATEX file prepared by the author.